Stacking faults, bound states, and quantum Hall plateaus in crystalline graphite

Daniel P. Arovas[1] and F. Guinea[2]
[1]*Department of Physics, University of California at San Diego, La Jolla, California 92093, USA*
[2]*Instituto de Ciencia de Materiales de Madrid, CSIC, Cantoblanco, E-28049 Madrid, Spain*
(Received 23 September 2008; revised manuscript received 17 November 2008; published 15 December 2008)

We analyze the electronic properties of a simple stacking defect in Bernal graphite. We show that a bound state forms, which disperses as $|\boldsymbol{k}-\boldsymbol{K}|^3$, in the vicinity of either of the two inequivalent zone corners $\boldsymbol{K}$. In the presence of a strong c-axis magnetic field, this bound state develops a Landau-level structure which for low energies behaves as $E_n \propto |nB|^{3/2}$. We show that buried stacking faults have observable consequences for surface spectroscopy, and we discuss the implications for the three-dimensional quantum Hall effect (3DQHE). We also analyze the Landau-level structure and chiral surface states of rhombohedral graphite and show that, when doped, it should exhibit multiple 3DQHE plateaus at modest fields.

DOI: 10.1103/PhysRevB.78.245416 PACS number(s): 81.05.Uw, 61.72.Nn, 73.43.−f

I. INTRODUCTION

An explosion of research activity associated with the novel two-dimensional material graphene[1] has prompted a re-examination of its bulk parent, graphite. Much, of course, is known about graphite.[2] Bernal graphite is a hexagonal crystal consisting of graphene sheets stacked in an *ABAB* configuration. The sp^2-hybridized σ electrons form double bonds between the carbon atoms, while the remaining π electrons, in the p^z orbital, are itinerant. The electronic structure parameters for graphite were first derived by Wallace and by Slonczewski, Weiss, and McClure (SWMC).[3] Within each plane, the π electrons move on a honeycomb lattice with a nearest-neighbor hopping integral $\gamma_0 \approx 3.2$ eV. Of the four atoms per unit cell, two are arranged in vertical chains, with a vertical nearest-neighbor hopping of $\gamma_1 \approx -390$ meV. Additional further neighbor hoppings are also present. For example, the π electrons on the nonchain sites undergo two-layer vertical hopping through open hexagons in the neighboring layers, with amplitude $\frac{1}{2}\gamma_2 \approx -10$ meV. This results in a very narrow band of width 40 meV along the *K*-*H* spine of the Brillouin zone, with electron pockets at *K* and hole pockets at *H*.[4]

Recently, striking experimental observations of what may be bulk three-dimensional (3D) quantum Hall plateaus in graphite have been reported.[14] Any two-dimensional (2D) system such as graphene, which exhibits the quantum Hall effect (QHE), should exhibit a three-dimensional quantum Hall effect (3DQHE) if the interplane coupling is sufficiently weak. The reason for this is that the cyclotron gaps between Landau levels narrow continuously as one adiabatically switches on the *c*-axis couplings and cannot collapse immediately. For a 3D electron system in a periodic potential and subjected to a magnetic field, a generalization of the Thouless-Kohmoto-Nightingale-den Nijs (TKNN) result[7] by Halperin[6] shows that the conductivity tensor must be of the form

$$\sigma_{ij} = \frac{e^2}{h}\epsilon_{ijk}G_k, \tag{1}$$

whenever the Fermi level E_F lies within a bulk gap, where ϵ_{ijk} is the fully antisymmetric tensor and $\vec{G}$ is a reciprocal-lattice vector of the potential (which may be $\vec{G}=0$). The Hall current is then carried by a sheath of chiral surface states. Eventually, however, the *c*-axis hopping will become large enough that the Landau gaps collapse. Equivalently, for a given value of the *c*-axis hopping γ_1, the magnetic field B must exceed a critical strength B_c in order that the Landau-level spacing overwhelms the *c*-axis bandwidth and opens up a bulk gap.

Typically, the field scale B_c is extremely large and much beyond the scale of current experimentally available fields. For a system with ballistic dispersion described by an effective mass m^*, the orbital part of the spectrum (i.e., neglecting Zeeman coupling) yields a dispersion $\varepsilon_n = (n+\frac{1}{2})\hbar\omega_c$, where n is a non-negative integer and where $\omega_c = eB/m^*c$ is the cyclotron frequency. The cyclotron energy may be written as $\hbar\omega_c = W_\parallel \cdot (B/B_\Omega)$ and the field scales as $B_\Omega = hc/e\Omega$, where Ω the unit-cell area. $W_\parallel$ is on the order of the bandwidth in zero field, which is typically several electron volts. Since $hc/e = 4.13 \times 10^5$ T Å^2, B_Ω is typically enormous, on the order of tens of thousands of tesla. Thus, if the *c*-axis bandwidth is $W_\perp$, the critical field is given by $B_c = (W_\perp/W_\parallel)\cdot B_\Omega$, and even highly anisotropic materials with $W_\perp \lesssim 10^{-2} W_\parallel$ will have critical fields in the range of hundreds of tesla.

As shown by Bernevig *et al.*,[5] similar considerations would apply for graphene sheets in *AAA* (simple hexagonal) stacking. The Landau-level dispersion is then

$$E_n(B,\boldsymbol{k}) = 2\gamma_1 \cos(k_z c) + \mathrm{sgn}(n)\gamma_0\sqrt{nB/B_0}, \tag{2}$$

with $B_0 = B_\Omega/2\pi\sqrt{3} = 7275$ T, where $\gamma_0 \approx 3.16$ eV is the in-plane hopping and $\gamma_1 \approx 0.39$ eV is the hopping integral between layers.[3] The gap between Landau levels n and $n+1$ collapses at a critical field

$$B_{c,n} = \left(\frac{4\gamma_1}{\gamma_0}\right)^2 \frac{B_0}{(\sqrt{n+1}-\sqrt{n})^2}. \tag{3}$$

For $n=0$ one finds $B_{c,0} \approx 1800$ T. However, due to the Bernal stacking, one finds[5] that the principal cyclotron gap surrounding the $n=0$ Landau levels opens above $B_c = 15$ T (electrons; $n=+1$) or above $B_c = 7$ T (holes; $n=-1$). When the Fermi level lies within either of these gaps, the Hall

conductance is quantized at $\sigma_{xy}=2e^2/hd$, where $d=3.37$ Å is the interplane separation.

The analysis of Ref. 5 shows that the second cyclotron gap should not open below fields on the order of $B_{c,2} \approx 1000$ T. This suggests that the multiple QHE plateaus observed by Kempa *et al.*[14] are of a different origin and are not describable by a model of crystalline Bernal graphite alone.

In this paper, we consider two variations which lead to a different plateau structure to that of crystalline Bernal graphite. The first is rhombohedral graphite (RG), which is stacked in *ABCABC* fashion. For this structure, we find

$$B_{c,n} = (\sqrt{n+1} + \sqrt{n})^2 B_{c,0},$$

with $B_{c,0} \approx 0.123$ T. When E_F lies in the Fermi level between the n and $n+1$ Landau levels, the Hall conductivity is given by $\sigma_{xy}=(4n+2)e^2/hd$. *Ab initio* calculations show the total energy of rhombohedral graphite to be approximately 0.11 meV per atom larger than the Bernal hexagonal phase.[8] With such a small energy difference, even highly oriented pyrolytic graphite (HOPG) is believed to contain several percent rhombohedral inclusions. Powdered graphite samples with up to ~40% of the rhombohedral phase are obtainable.[9]

The second possibility we examine is that of a simple stacking fault in Bernal graphite of the form *ABABCBCB*. This fault interpolates between two degenerate vacua: the *ABAB* and *CBCB* Bernal phases. We analyze the *c*-axis transport through such a defect, within a simple model of nearest-neighbor hopping and compute the *S* matrix as a function of in-plane wave vector. As expected, the transmission is sharply attenuated in the vicinity of the Dirac points. We also find a different bound state associated with the stacking defect, with two-dimensional dispersion $E(\boldsymbol{k}) \propto |\boldsymbol{k}-\boldsymbol{K}|^3$ near the Dirac points. In the presence of a *c*-axis magnetic field, this leads to a bound-state Landau-level energy $E(n,B) \propto |nB|^{3/2}$. In the Appendix, we undertake a calculation of the bound-state spectrum in zero field for the full SWMC model,[3] which includes seven tight-binding parameters. We conclude with a discussion of surface spectroscopy of buried stacking faults and with remarks about the relevance of our results to future experiments.

II. RHOMBOHEDRAL GRAPHITE

In RG there are two sublattices (Fig. 1), in contrast to four in the case of Bernal hexagonal graphite (BHG). The primitive direct lattice vectors are

$$\boldsymbol{a}_1 = a\hat{\boldsymbol{x}},$$

$$\boldsymbol{a}_2 = \frac{1}{2}a\hat{\boldsymbol{x}} + \frac{\sqrt{3}}{2}a\hat{\boldsymbol{y}},$$

$$\boldsymbol{a}_3 = \frac{1}{2}a\hat{\boldsymbol{x}} + \frac{1}{2\sqrt{3}}a\hat{\boldsymbol{y}} + d\hat{\boldsymbol{z}}.$$

The basis vector $\boldsymbol{\delta}=-\frac{1}{3}(\boldsymbol{a}_1+\boldsymbol{a}_2)$ separates the *A* and *B* sublattices. Note that $\boldsymbol{a}_3=d\hat{\boldsymbol{z}}-\boldsymbol{\delta}$. The lattice parameters are $a=2.46$ Å and $d=3.37$ Å.

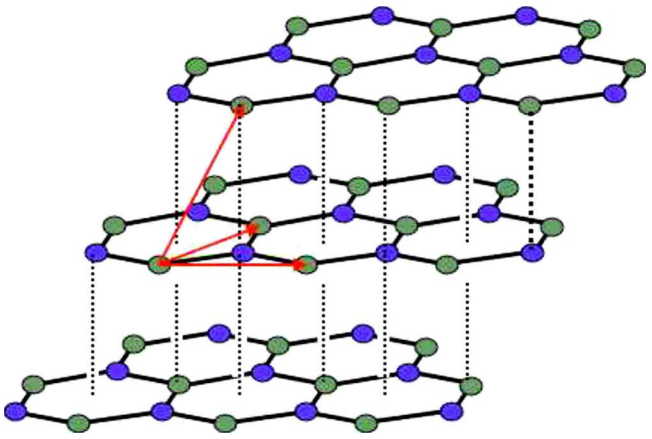

FIG. 1. (Color online) Crystal structure of rhombohedral graphite.

Our treatment starts with a simplified version of the work of McClure.[10] We consider several types of hopping processes as follows:

(i) in-plane *A*-*B* hopping

$$H_1^{AB} = -\gamma_0[t(\boldsymbol{\delta}) + t(\boldsymbol{a}_1+\boldsymbol{\delta}) + t(\boldsymbol{a}_2+\boldsymbol{\delta})], \tag{4}$$

where, $t(\boldsymbol{d})$ is a translation operator through a vector $\boldsymbol{d}$;

(ii) neighboring plane diagonal *A*-*B* hopping

$$H_2^{AB} = \gamma_3[t(\boldsymbol{a}_1-\boldsymbol{a}_3+\boldsymbol{\delta}) + t(\boldsymbol{a}_2-\boldsymbol{a}_3+\boldsymbol{\delta}) + t(\boldsymbol{a}_1+\boldsymbol{a}_2-\boldsymbol{a}_3+\boldsymbol{\delta})], \tag{5}$$

(iii) nearest-neighbor and next-nearest-neighbor plane vertical *A*-*B* hopping

$$H_3^{AB} = \gamma_1 t(\boldsymbol{a}_3+\boldsymbol{\delta}) + \gamma_2 t(\boldsymbol{a}_1+\boldsymbol{a}_2-2\boldsymbol{a}_3+\boldsymbol{\delta}), \tag{6}$$

(iv) neighboring plane diagonal *A*-*A* hopping

$$H_4^{AA} = \gamma_3[t(\boldsymbol{a}_3) + t(\boldsymbol{a}_3-\boldsymbol{a}_1) + t(\boldsymbol{a}_3-\boldsymbol{a}_2)] + \text{H.c.}, \tag{7}$$

(v) neighboring plane diagonal *B*-*B* hopping

$$H_4^{BB} = \gamma_3[t(\boldsymbol{a}_3) + t(\boldsymbol{a}_3-\boldsymbol{a}_1) + t(\boldsymbol{a}_3-\boldsymbol{a}_2)] + \text{H.c.} \tag{8}$$

The full Hamiltonian is then given by

$$H = \begin{pmatrix} H_4^{AA} & H_1^{AB}+H_2^{AB}+H_3^{AB} \\ H_1^{BA}+H_2^{BA}+H_3^{BA} & H_4^{BB} \end{pmatrix}, \tag{9}$$

where $H_n^{BA}=(H_n^{AB})^\dagger$ for $n=1,2,3$. From Wallace and SWMC,[3,12] we take

$$\gamma_0 = 3160 \text{ meV}, \quad \gamma_1 = 390 \text{ meV},$$

$$\gamma_2 = 10 \text{ meV}, \quad \gamma_3 = 250 \text{ meV}.$$

(In the language of McClure,[10] $\gamma_2'=\gamma_2$ and $\gamma_1'=\gamma_3$, and we ignore McClure's parameters γ_0' and γ_2''.) We then have

$$H = \begin{pmatrix} \eta & 0 \\ 0 & 1 \end{pmatrix} \begin{pmatrix} A & B \\ B^* & A \end{pmatrix} \begin{pmatrix} \eta^* & 0 \\ 0 & 1 \end{pmatrix}, \tag{10}$$

with $\eta=e^{i(\theta_1+\theta_2)/3}$ and

$$A(\theta_1,\theta_2,\theta_3) = \gamma_3 e^{-i\theta_3} T(\theta_1,\theta_2) + \gamma_3 e^{i\theta_3} T^*(\theta_1,\theta_2),$$

$$B(\theta_1,\theta_2,\theta_3) = -\gamma_0 T(\theta_1,\theta_2) + \gamma_3 e^{-i\theta_3} T^*(\theta_1,\theta_2) + \gamma_1 e^{i\theta_3} + \gamma_2 e^{i(\theta_1+\theta_2-2\theta_3)},$$

where

$$T(\theta_1,\theta_2) = 1 + e^{i\theta_1} + e^{i\theta_2}. \tag{11}$$

The energy eigenvalues are clearly

$$E_\pm(\boldsymbol{\theta}) = A(\boldsymbol{\theta}) \pm |B(\boldsymbol{\theta})|. \tag{12}$$

Under a 60° rotation, we have

$$\theta_1' = \theta_2, \quad \theta_2' = \theta_2 - \theta_1, \quad \theta_3' = \theta_2 - \theta_3. \tag{13}$$

One then finds $A(\boldsymbol{\theta}')=A(\boldsymbol{\theta})$ and $B(\boldsymbol{\theta}')=e^{i\theta_2}B(\boldsymbol{\theta})$. Hence, $E_\pm(\boldsymbol{\theta}')=E_\pm(\boldsymbol{\theta})$.

Degeneracies identified with a one-parameter family of Dirac points occur when $B(\boldsymbol{\theta})=0$. Solving, we obtain the relation

$$T(\theta_1,\theta_2) = \Gamma_1 e^{i\theta_3} + \Gamma_2 e^{i(\theta_1+\theta_2-2\theta_3)} \tag{14}$$

along the degeneracy curve, where

$$\Gamma_1 \equiv \frac{\gamma_0\gamma_1 + \gamma_2\gamma_3}{\gamma_0^2 - \gamma_3^2} = -0.124, \tag{15}$$

$$\Gamma_2 \equiv \frac{\gamma_1\gamma_3 + \gamma_0\gamma_2}{\gamma_0^2 - \gamma_3^2} = -1.30 \times 10^{-2}. \tag{16}$$

The energy along this Dirac curve is

$$E(\boldsymbol{\theta}_D) = \mathcal{E}_0 + W\cos(\theta_1 + \theta_2 - 3\theta_3). \tag{17}$$

with

$$\mathcal{E}_0 = 2\Gamma_1\gamma_3 = -62 \text{ meV}, \tag{18}$$

$$W = 2\Gamma_2\gamma_3 = -6.5 \text{ meV}. \tag{19}$$

Since Γ_1 and Γ_2 are small, the Dirac curve, when projected into the basal Brillouin zone, lies close to the zone corners. Note that $E(\boldsymbol{\theta}_D)$ goes through three complete periods as θ_3 advances from 0 to 2π, resulting in McClure's "sausage link" Fermi surface,[10] depicted in Fig. 2. To find the equation of the Dirac curve, we expand about $\boldsymbol{\Theta}=(\theta_1,\theta_2)=(\frac{4\pi}{3},\frac{2\pi}{3})$ at the K point, writing $\boldsymbol{\theta}=\boldsymbol{\Theta}+\boldsymbol{\zeta}$, and find

$$T(\Theta_1+\delta\theta_1,\Theta_2+\delta\theta_2) = e^{-i\pi/6}\delta\theta_1 - e^{i\pi/6}\delta\theta_2 + \mathcal{O}(\delta\theta^2). \tag{20}$$

Solving for the Dirac line $\boldsymbol{\zeta}(\theta_3)$ as a formal series in the small parameters Γ_1 and Γ_2, we obtain

$$\delta\theta_1 = \frac{2}{\sqrt{3}}\left[-\Gamma_1\sin\left(\theta_3 - \frac{\pi}{6}\right) + \Gamma_2\sin\left(2\theta_3 + \frac{\pi}{6}\right)\right] + \mathcal{O}(\Gamma^2),$$

$$\delta\theta_2 = \frac{2}{\sqrt{3}}\left[\Gamma_1\sin\left(\theta_3 + \frac{\pi}{6}\right) - \Gamma_2\sin\left(2\theta_3 - \frac{\pi}{6}\right)\right] + \mathcal{O}(\Gamma^2).$$

Note that the bandwidth of the Dirac point energies is tiny; $2W \approx 13$ meV. This means that the Landau levels are quite narrow, more so than in Bernal stacked graphite. The Fermi surface resembles the sketch in Fig. 2, which is adapted from Fig. 2 of Ref. 10.

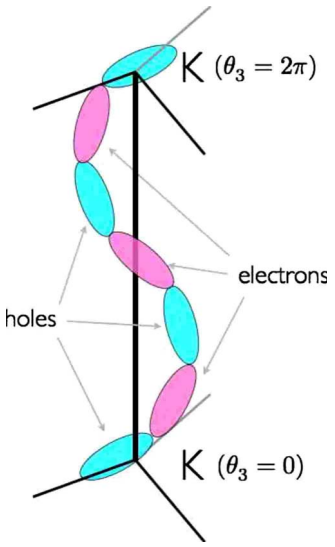

FIG. 2. (Color online) McClure's sausage link Fermi surface for rhombohedral graphite, greatly exaggerated. See also Fig. 2 of Ref. 10.

A. Weak fields: Kohn-Luttinger substitution

We assume the magnetic field **B** is directed along $\hat{z}$. To obtain the Landau levels, we expand about the Dirac points. (This is essentially equivalent to expanding about the Fermi energy since the bandwidth of the Dirac points is so tiny.) We write

$$\boldsymbol{k} \to \boldsymbol{K} + \hbar^{-1}\boldsymbol{\pi}, \tag{21}$$

where $\boldsymbol{\pi}=\boldsymbol{p}+\frac{e}{c}\boldsymbol{A}$. With $\delta\theta_j=(\boldsymbol{k}-\boldsymbol{K})\cdot\boldsymbol{a}_j$, we have

$$\delta\theta_1 = \frac{1}{\hbar}\pi_x a, \tag{22}$$

$$\delta\theta_2 = \frac{1}{2\hbar}\pi_x a + \frac{\sqrt{3}}{2\hbar}\pi_y a. \tag{23}$$

Recall $[\pi_x,\pi_y]=-i\hbar^2/\ell_B^2$ where $\ell_B=\sqrt{\hbar c/eB}$ is the magnetic length. From Eq. (20), to the lowest order in $\delta\theta_{1,2}$, we have

$$[T,T^\dagger] = 2i\sin(\pi/3)[\delta\theta_1,\delta\theta_2] = 2\pi\sqrt{3}p/q, \tag{24}$$

where the flux per unit-cell area $\Omega=\frac{\sqrt{3}}{2}a^2$ is assumed to be a rational multiple p/q of the Dirac flux quantum $\phi_0=hc/e$. This means that we may write

$$T(\theta_1,\theta_2) = -\epsilon b, \tag{25}$$

where

$$\epsilon = \sqrt{B/B_0} \tag{26}$$

and $b^\dagger$ is a Landau-level raising operator; $[b,b^\dagger]=1$. Recall that the field scale $B_0=(hc/e)/3\pi a^2=7275$ T. It is conve-

nient to define $\bar{\theta}_3 = \theta_3 - \frac{1}{3}(\theta_1 + \theta_2)$ and to absorb a phase into the definition of b, taking $T = -\epsilon e^{-i\bar{\theta}_3} b^\dagger$. Note that when the magnetic field lies along the c axis, it is $\exp(i\bar{\theta}_3)$ and not $\exp(i\theta_3)$ which commutes with the magnetic translations $t(\boldsymbol{a}_{1,2})$. The Hamiltonian is then

$$H = \mathcal{E}_0 + W\cos(3\bar{\theta}_3) \tag{27}$$

$$+ \epsilon \begin{pmatrix} -\gamma_3(b+b^\dagger) & \gamma_0 e^{-i\bar{\theta}_3} b^\dagger - \gamma_3 b \\ \gamma_0 e^{i\bar{\theta}_3} b - \gamma_3 b^\dagger & -\gamma_3(b+b^\dagger) \end{pmatrix}. \tag{28}$$

Consider the matrix operators

$$\mathcal{Q}_0 = \gamma_0 \begin{pmatrix} 0 & e^{-i\bar{\theta}_3} b^\dagger \\ e^{i\bar{\theta}_3} b & 0 \end{pmatrix}, \tag{29}$$

$$\mathcal{Q}_1 = \gamma_3 \begin{pmatrix} b+b^\dagger & b \\ b^\dagger & b+b^\dagger \end{pmatrix}. \tag{30}$$

The eigenvectors of $\mathcal{Q}_0$ are

$$|\Psi_0\rangle = \begin{pmatrix} |0\rangle \\ 0 \end{pmatrix}, \quad E_0^0 = 0 \tag{31}$$

and

$$|\Psi_n^\pm\rangle = \frac{1}{\sqrt{2}} \begin{pmatrix} e^{-i\bar{\theta}_3}|n\rangle \\ \pm|n-1\rangle \end{pmatrix}, \quad E_n^0 = \pm\sqrt{n}\epsilon\gamma_0, \tag{32}$$

where $n = 1, 2, 3, \ldots$. It is easy to see that

$$\langle \Psi_n^\pm | \mathcal{Q}_1 | \Psi_n^\pm \rangle = 0, \tag{33}$$

as well as $\langle\Psi_0|\mathcal{Q}_1|\Psi_0\rangle = 0$; hence, there is no first-order shift of the eigenvalues. Therefore, up to first order in ϵ, the Landau-level energies are given by

$$E_n(\theta_3) = \mathcal{E}_0 + W\cos(3\bar{\theta}_3) \pm \epsilon\gamma_0\sqrt{n}, \tag{34}$$

where $n = 0, 1, 2, \ldots$. The gap between Landau levels n and $n+1$ collapses when

$$\epsilon\gamma_0\sqrt{n} + W = \epsilon\gamma_0\sqrt{n+1} - W, \tag{35}$$

which gives a critical field of

$$B_{c,n} = (\sqrt{n+1} + \sqrt{n})^2 B_{c,0}, \tag{36}$$

with $B_{c,0} = (2W/\gamma_0)^2 \cdot B_0 = 0.123$ T.

B. Comparison with Bernal stacking

The *ABAB* stacking pattern of Bernal hexagonal graphite is shown in Fig. 3. To obtain the critical fields in BHG, it suffices to consider a simple nearest-neighbor model.[5] Expanding about the *K-H* spine in the Brillouin zone, we obtain in the presence of a uniform c-axis magnetic field

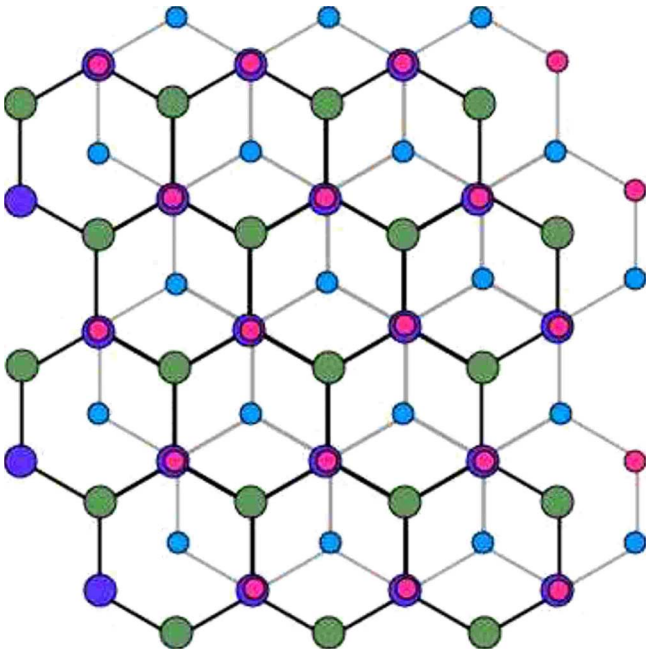

FIG. 3. (Color online) Top view of Bernal hexagonal graphite.

$$H = \begin{pmatrix} 0 & \epsilon\gamma_0 b & 2\gamma_1\cos\theta_3 & 0 \\ \epsilon t_\parallel b^\dagger & 0 & 0 & 0 \\ 2\gamma_1\cos\theta_3 & 0 & 0 & -\epsilon\gamma_0 b^\dagger \\ 0 & 0 & \epsilon\gamma_0 b & 0 \end{pmatrix}, \tag{37}$$

where $\epsilon = (2\pi\sqrt{3}p/q)^{1/2} = \sqrt{B/B_0}$ as in the rhombohedral case (Fig. 4). The spectrum has explicit particle-hole symmetry. For $n = 0$ there are eigenvalues at $\pm(\epsilon^2\gamma_0^2 + 4\gamma_1^2\cos^2\theta_3)^{1/2}$

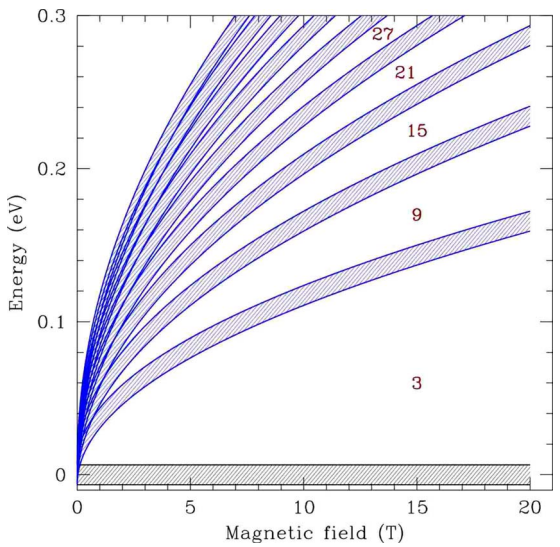

FIG. 4. (Color online) Landau-level structure in rhombohedral graphite within the tight-binding model of Sec. II, with Zeeman term ignored. Principal band gaps are labeled by the Chern number C (per spin degree of freedom). When E_F lies within a gap, the Hall conductivity is $2C \times \frac{e^2}{h}/3d$, where $d = 3.37$ Å is the interplane spacing.

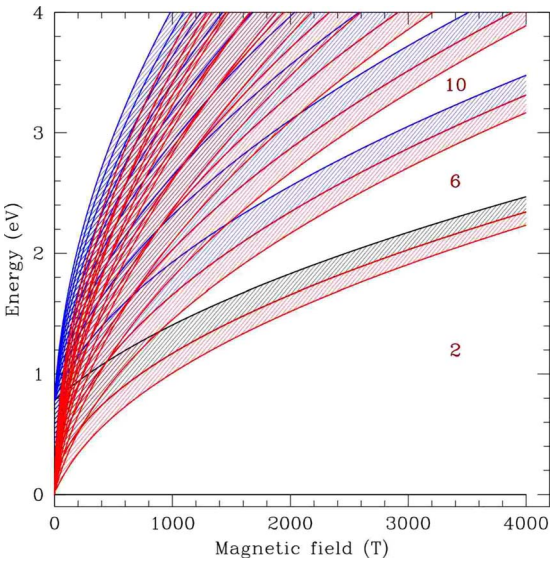

FIG. 5. (Color online) Landau-level structure in Bernal graphite within the nearest-neighbor hopping model, with Zeeman term ignored. Principal band gaps are labeled by the Chern number C (per spin degree of freedom). When E_F lies within a gap, the Hall conductivity is $2C\times\frac{e^2}{h}/2d$. When further neighbor hoppings are included, particle-hole symmetry is broken and a finite field is required to open the principal gap (Ref. 5).

and a doubly degenerate level at $E_0=0$. For $n\neq 0$,

$$E_n^2=\left(n+\tfrac{1}{2}\right)\epsilon^2\gamma_0^2+2\gamma_1^2\cos^2\theta_3 \pm\sqrt{\tfrac{1}{4}\epsilon^4\gamma_0^4+4\left(n+\tfrac{1}{2}\right)\epsilon^2\gamma_0^2\gamma_1^2\cos^2\theta_3+4\gamma_1^4\cos^4\theta_3}. \tag{38}$$

In Fig. 5, we plot the lowest several energy bands versus magnetic field for BHG. Due to the inadequacies of the nearest-neighbor model, the principal gap surrounding central $E=0$ Landau levels opens immediately for nonzero B. Including more realistic band-structure effects, consistent with the semimetallic nature of BHG, this gap opens at a critical field of $B_c\approx 15$ T for positive energies and $B_c\approx 7$ T for negative energies.[5] The Hall conductance is quantized at $\sigma_{xy}=2Ce^2/hc_0$ when the Fermi level lies in a bulk gap, where $c_0=2d$ in BHG and $c_0=3d$ in RG, where $d=3.37$ Å is the spacing between planes, and C is a topological integer associated with the gap. In both cases, the values of C are such that σ_{xy} corresponds to the graphene quantization per layer, changing by $4e^2/hd$ as one crosses a Landau level. We indicate the width of the bands by shading the region between $\cos^2\theta_0=0$ and $\cos^2\theta_3=1$. In both cases, the Zeeman coupling is omitted; with $g\approx 2$ the Zeeman splitting is small compared with the cyclotron energy.

III. CHIRAL SURFACE STATES

As shown by Hatsugai,[11] the Chern number C can also be computed by following the spectral flow in a system with edges, wrapped around a cylinder, as a function of the gauge flux through the cylinder. To elicit this spectral flow, we derive a Hofstadter Hamiltonian[13] for RG. We start with the Hamiltonian elements in Sec. II, but now treating them as magnetic translations, which satisfy the algebra

$$t(\mathbf{a})t(\mathbf{b})=e^{i\mathbf{a}\times\mathbf{b}\cdot\hat{\mathbf{n}}/2\ell_B^2}t(\mathbf{a}+\mathbf{b}), \tag{39}$$

where $\mathbf{B}=B\hat{\mathbf{n}}$. For our problem we define the elementary translations

$$t_1\equiv t(\mathbf{ffi}),\quad t_2\equiv t(\mathbf{a}_1+\mathbf{ffi}) \tag{40}$$

as well as $\tau\equiv t(d\hat{\mathbf{z}})=t(\mathbf{a}_3+\mathbf{ffi})$.

Since with $\hat{\mathbf{n}}=\hat{\mathbf{z}}$ we have that τ commutes with t_1 and t_2, and we can specify its eigenvalue as $e^{i\bar{\theta}_3}$. As for $t_{1,2}$, we have

$$t_1t_2=e^{i\phi/3}t_2t_1, \tag{41}$$

where $\phi=\Omega/\ell_B^2=2\pi p/q$ is the flux per graphene hexagon in units of $\hbar c/e$. We may then write

$$H=\begin{pmatrix}H_{AA} & H_{AB}\\ H_{AB}^\dagger & H_{BB}\end{pmatrix}, \tag{42}$$

with

$$H_{AA}=\gamma_3(e^{i\bar{\theta}_3}t_1+e^{-i\bar{\theta}_3}t_1^\dagger)+\gamma_3(e^{i\bar{\theta}_3}+e^{-i\bar{\theta}_3}e^{-i\phi/6}t_1)t_2 +\gamma_3(e^{-i\bar{\theta}_3}+e^{i\bar{\theta}_3}e^{-i\phi/6}t_1^\dagger)t_2^\dagger=H_{BB} \tag{43}$$

and

$$H_{AB}=(\gamma_1e^{i\bar{\theta}_3}+\gamma_2e^{-2i\bar{\theta}_3}-\gamma_0t_1^\dagger+\gamma_3e^{-i\bar{\theta}_3}t_1) +(\gamma_3e^{-i\bar{\theta}_3}-\gamma_0e^{-i\phi/6}t_1)t_2-(\gamma_0-\gamma_3e^{i\bar{\theta}_3}e^{-i\phi/6}t_1^\dagger)t_2^\dagger. \tag{44}$$

We define the basis $\{|n\rangle\}$ as follows:

$$t_1|n\rangle=e^{i\bar{\theta}_1}e^{in\phi/3}|n\rangle, \tag{45}$$

$$t_2|n\rangle=e^{i\theta_2}|n+1\rangle, \tag{46}$$

where $\bar{\theta}_1=\theta_1/3q$ and $|n+3q\rangle=|n\rangle$. Taking the matrix elements of H within this basis, one obtains a rank $6q$ matrix H to diagonalize, with periodic boundary conditions. If we introduce an edge by eliminating the coupling between states $|1\rangle$ and $|3q\rangle$ and plot the spectral flow as a function of $\bar{\theta}_1$, we obtain the top panel in Fig. 6. We can also obtain the chiral surface-state flow for a zigzag edge, perpendicular to the vector $\mathbf{a}_1$; this is shown in the bottom panel of Fig. 6. For periodic systems, exact diagonalizations performed using the Lanczos method for q up to 1500 with the package ARPACK were found to agree with the weak field results of Sec. II A.

IV. STACKING FAULTS IN BERNAL HEXAGONAL GRAPHITE

We now turn to an analysis of simple stacking faults in BHG, first with $\mathbf{B}=0$ and then for finite $\mathbf{B}$. Consider first a triangular lattice, which is tripartite, and its three triangular sublattices A, B, and C. By eliminating one of these three sublattices, the remaining structure will be a honeycomb lattice. Now imagine a stack of triangular lattices. At each

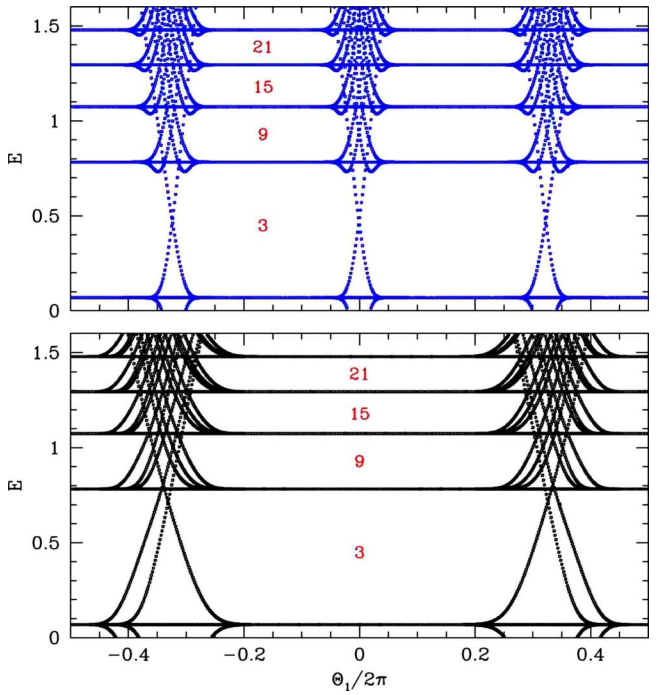

FIG. 6. (Color online) Spectral flow in rhombohedral graphite showing edge state evolution. Top panel: armchair edge perpendicular to **ffi**; bottom panel: zigzag edge perpendicular to $\mathbf{a}_1$. The bulk gaps are labeled by Chern numbers C which correspond to the number of edge states crossing the gap as the angle θ_1 is varied. The flux per unit cell here is rather large, with $p=1$ and $q=200$, corresponding to a field of $B=396$ T. The topological features of the edge state spectral flow are robust with respect to field.

layer, we choose a sublattice A, B, or C to remove; this defines a stacking pattern. Since it is energetically unfavorable to stack a honeycomb layer directly atop another, at each layer we have two choices consistent with the layer below. If the empty sublattices are in *ABC et cyc.* order from layer l to layer $l+1$, we write $\sigma_{n,n+1}=+1$. If instead the order is *CBA et cyc.*, we write $\sigma_{l,l+1}=-1$. For RG, the σ indices are "ferromagnetic," i.e., $++++$ or $----$. For BHG, the indices are ordered "antiferromagnetically," i.e., $+-+-$.

The three triangular sublattices A, B, and C are defined by

$$u^A_{n_1,n_2} = n_1\mathbf{a}_1 + n_2\mathbf{a}_2, \tag{47}$$

$$u^B_{n_1,n_2} = n_1\mathbf{a}_1 + n_2\mathbf{a}_2 + \mathbf{ffi}_1, \tag{48}$$

$$u^C_{n_1,n_2} = n_1\mathbf{a}_1 + n_2\mathbf{a}_2 + 2\mathbf{ffi}_1. \tag{49}$$

We define three additional sublattices by

$$v^A_{n_1,n_2} = u^B_{n_1,n_2} = n_1\mathbf{a}_1 + n_2\mathbf{a}_2 + \mathbf{ffi}_1, \tag{50}$$

$$v^B_{n_1,n_2} = u^C_{n_1,n_2} = n_1\mathbf{a}_1 + n_2\mathbf{a}_2 + 2\mathbf{ffi}_1, \tag{51}$$

$$v^C_{n_1,n_2} = u^A_{n_1,n_2} = n_1\mathbf{a}_1 + n_2\mathbf{a}_2. \tag{52}$$

The sites $\{u_A(n_1,n_2), v_A(n_1,n_2)\}$, etc. form a honeycomb lattice, which we call the A or α structure. Bernal graphite is stacked in an *ABABAB* configuration.

Within each honeycomb layer, we write the wave function as a two-component spinor,

$$\psi_{\mathbf{k}} = \begin{pmatrix} u_{\mathbf{k}} \\ v_{\mathbf{k}} \end{pmatrix}, \tag{53}$$

where $\mathbf{k}$ is the crystal momentum in the basal ($k_z=0$) Brillouin zone.

The hopping between planes is described by the following local Schrödinger equation, which couples a central plane l to planes below $(l-1)$ and above $(l+1)$,

$$M\psi_l + \gamma_1(\Sigma^\sigma)^\dagger\psi_{l-1} + \gamma_1\Sigma^{\sigma'}\psi_{l+1} = 0. \tag{54}$$

Here, $\sigma_{l-1,l}=\sigma$ and $\sigma_{l,l+1}=\sigma'$, i.e., the shift in the u sublattice sites from plane $l-1$ to plane l is through a vector $\sigma\mathbf{ffi}_1$. The matrix M is given by

$$M = \begin{pmatrix} E & \gamma_0 S \\ \gamma_0 S^* & E \end{pmatrix}, \tag{55}$$

and

$$S = e^{i\mathbf{k}\cdot\mathbf{ffi}_1} + e^{i\mathbf{k}\cdot\mathbf{ffi}_2} + e^{i\mathbf{k}\cdot\mathbf{ffi}_3} \tag{56}$$

and

$$\Sigma^+ = \begin{pmatrix} 0 & 1 \\ 0 & 0 \end{pmatrix}, \quad \Sigma^- = \begin{pmatrix} 0 & 0 \\ 1 & 0 \end{pmatrix}. \tag{57}$$

A. Bernal hexagonal graphite

We first consider the BHG stacking order *ABABAB*, where $\sigma_{l,l+1}=(-1)^l$. Using translational invariance, we may write, for the even and odd sites

$$\psi_{2j} = e^{2ijk_zd}\phi, \tag{58}$$

$$\psi_{2j+1} = e^{i(2j+1)k_zd}\chi, \tag{59}$$

where

$$M\phi + 2\gamma_1\cos(k_zd)\Sigma^-\chi = 0, \tag{60}$$

$$M\chi + 2\gamma_1\cos(k_zd)\Sigma^+\phi = 0. \tag{61}$$

Inverting the second of these equations gives

$$\chi = -2\gamma_1\cos(k_zd)M^{-1}\Sigma^+\phi. \tag{62}$$

Substituting this into the first equation yields

$$[M - 4\gamma_1^2\cos^2(k_zd)\Sigma^-M^{-1}\Sigma^+]\phi = 0. \tag{63}$$

Accordingly, we define

$$\mathcal{K} \equiv M - 4\gamma_1^2\cos^2(k_zd)\Sigma^-M^{-1}\Sigma^+ \tag{64}$$

$$= \begin{pmatrix} E & \gamma_0 S \\ \gamma_0 S^* & E\left(1 - \dfrac{4\gamma_1^2 \cos^2(k_z d)}{E^2 - \gamma_0^2 |S|^2}\right) \end{pmatrix}. \tag{65}$$

Setting $\det \mathcal{K} = 0$ yields the eigenvalue equation for Bernal graphite,

$$(E^2 - \gamma_0^2 |S|^2)^2 - 4E^2 \gamma_1^2 \cos^2(k_z d) = 0, \tag{66}$$

with solutions

$$E_{\mathbf{k},k_z}^{(\mu,\mu')} = -\mu \gamma_1 \cos(k_z d) - \mu' \sqrt{\gamma_1^2 \cos^2(k_z d) + \gamma_0^2 |S|^2}, \tag{67}$$

where $\mu = \pm 1$ and $\mu' = \pm 1$. The four choices for (μ, μ') correspond to the four energy bands.

From $\mathcal{K}\phi = 0$, we may write

$$\phi = \begin{pmatrix} \phi_1 \\ \phi_2 \end{pmatrix} = \begin{pmatrix} -\gamma_0 S \\ E \end{pmatrix}. \tag{68}$$

From Eq. (62), then, we have

$$\chi = \begin{pmatrix} \chi_1 \\ \chi_2 \end{pmatrix} = \frac{2E\gamma_1 \cos(k_z d)}{E^2 - \gamma_0^2 |S|^2} \begin{pmatrix} -E \\ \gamma_0 S^* \end{pmatrix} = \mu \begin{pmatrix} E \\ -\gamma_0 S^* \end{pmatrix}. \tag{69}$$

B. Step defect

Consider now the stacking defect *ABABCBCB*, which in terms of the $\sigma_{l,l+1}$ variables may be depicted as

$$\cdots | + | - | + | - | - | + | - | + | \cdots. \tag{70}$$

We label the central plane as $l = 0$. For plane indices $l < 0$, the odd layers correspond to ϕ planes and the even layers to χ planes. For $l > 0$, the even layers correspond to ϕ planes and the odd layers to χ planes. With $l < 0$, we consider an incident plane wave running to the right (up) and a reflected plane wave running to the left (down). Then we have

$$\psi_{2j} = (\alpha e^{2ijk_z d} + \beta' e^{-2ijk_z d})\chi, \tag{71}$$

$$\psi_{2j+1} = (\alpha e^{i(2j+1)k_z d} + \beta' e^{-i(2j+1)k_z d})\phi, \tag{72}$$

for all $j < 0$. Here α is the complex amplitude of the incident wave and β' is the complex amplitude of the reflected wave.

Correspondingly, we have

$$\psi_{2j-1} = (\beta e^{i(2j-1)k_z d} + \alpha' e^{-i(2j-1)k_z d})\chi, \tag{73}$$

$$\psi_{2j} = (\beta e^{2ijk_z d} + \alpha' e^{-2ijk_z d})\phi, \tag{74}$$

for all $j > 0$. Here α' is the incident amplitude (from the right/top) and β is the reflected amplitude.

To match the solutions for positive and negative l, we first invoke Eq. (54) with $l = -1$,

$$M\psi_{-1} + \gamma_1 \Sigma^- \psi_{-2} + \gamma_1 \Sigma^- \psi_0 = 0. \tag{75}$$

The most general solution for ψ_0 is then

$$\psi_0 = (\alpha + \beta')\chi + \begin{pmatrix} 0 \\ b \end{pmatrix}, \tag{76}$$

where b is an arbitrary complex number. Note that Σ^- annihilates any vector with upper component 0.

Next, set $l = +1$ and obtain

$$M\psi_1 + \gamma_1 \Sigma^+ \psi_0 + \gamma_1 \Sigma^+ \psi_2 = 0. \tag{77}$$

We may now write

$$\psi_0 = (\beta + \alpha')\phi + \begin{pmatrix} a \\ 0 \end{pmatrix}, \tag{78}$$

where a is an arbitrary complex parameter. Note that Σ^+ annihilates any vector with lower component 0.

The parameters a and b are then fixed by equating these two expressions for ψ_0, yielding

$$\begin{pmatrix} a \\ -b \end{pmatrix} = (\alpha + \beta')\chi - (\beta + \alpha')\phi. \tag{79}$$

The wave function at $l = 0$ can now be found. One simple way is to take the upper component from Eq. (76) and the lower component from Eq. (78),

$$\psi_0 = \begin{pmatrix} (\alpha + \beta')\chi_1 \\ (\beta + \alpha')\phi_2 \end{pmatrix}. \tag{80}$$

Next, we write the Schrödinger equation for the $l = 0$ plane as follows:

$$\begin{aligned} 0 &= M\psi_0 + \gamma_1 \Sigma^+ \psi_{-1} + \gamma_1 \Sigma^- \psi_{+1} \\ &= \begin{pmatrix} E & \gamma_0 S \\ \gamma_0 S^* & E \end{pmatrix} \begin{pmatrix} (\alpha + \beta')\chi_1 \\ (\beta + \alpha')\phi_2 \end{pmatrix} + \gamma_1 (\alpha e^{-ik_z d} + \beta' e^{ik_z d}) \begin{pmatrix} \phi_2 \\ 0 \end{pmatrix} \\ &\quad + \gamma_1 (\beta e^{ik_z d} + \alpha' e^{-ik_z d}) \begin{pmatrix} 0 \\ \chi_1 \end{pmatrix}. \end{aligned} \tag{81}$$

This yields two equations which may be solved to relate the outgoing amplitudes β and β' to the incoming amplitudes α and α', i.e., to derive the $\mathcal{S}$ matrix. Using our previously derived results for ϕ and χ, we find that the above equation reduces to

$$0 = \begin{pmatrix} E & \gamma_0 S \\ \gamma_0 S^* & E \end{pmatrix} \begin{pmatrix} \mu(\alpha + \beta') \\ (\beta + \alpha') \end{pmatrix} + \gamma_1 \begin{pmatrix} (\alpha e^{-ik_z d} + \beta' e^{ik_z d}) \\ \mu(\beta e^{ik_z d} + \alpha' e^{-ik_z d}) \end{pmatrix}. \tag{82}$$

This yields

$$\begin{aligned} 0 &= \begin{pmatrix} \mu E + \gamma_1 e^{-i\theta_z/2} & \gamma_0 S \\ \mu \gamma_0 S^* & E + \mu \gamma_1 e^{-i\theta_z/2} \end{pmatrix} \begin{pmatrix} \alpha \\ \alpha' \end{pmatrix} \\ &\quad + \begin{pmatrix} \gamma_0 S & \mu E + \gamma_1 e^{i\theta_z/2} \\ E + \mu \gamma_1 e^{-i\theta_z/2} & \mu \gamma_0 S^* \end{pmatrix} \begin{pmatrix} \beta \\ \beta' \end{pmatrix}, \end{aligned} \tag{83}$$

where $\theta_z \equiv 2k_z d$. The $\mathcal{S}$ matrix is defined by

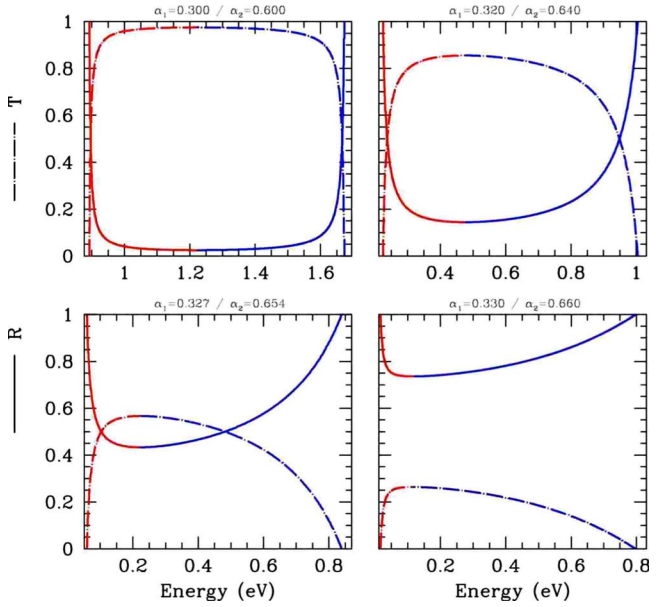

FIG. 7. (Color online) Reflection and transmission coefficients for $\mathbf{k}=\alpha_1\mathbf{b}_1+\alpha_2\mathbf{b}_2$, for four sets of (α_1,α_2), in the vicinity of the Dirac point $(\frac{1}{3},\frac{2}{3})$. Only positive energies are shown.

$$\begin{pmatrix}\beta\\ \beta'\end{pmatrix}=\overbrace{\begin{pmatrix}t & r'\\ r & t'\end{pmatrix}}^{\mathcal{S}\ \text{matrix}}\begin{pmatrix}\alpha\\ \alpha'\end{pmatrix}. \tag{84}$$

Solving for $\mathcal{S}$, we obtain

$$\mathcal{S}=\frac{-\begin{pmatrix}2i\gamma_0 S^*\sin(\theta_z/2) & \gamma_1\\ \gamma_1 & 2i\gamma_0 S\sin(\theta_z/2)\end{pmatrix}}{\gamma_1\cos(\theta_z)+2i\mu\sin(\theta_z/2)[\gamma_1^2\cos^2(\theta_z/2)+\gamma_0^2|S|^2]^{1/2}}. \tag{85}$$

Thus, for all μ and μ', we have

$$R=|r|^2=\frac{\gamma_1^2}{\gamma_1^2+4\gamma_0^2|S|^2\sin^2(\theta_z/2)}, \tag{86}$$

and

$$T=|t|^2=\frac{4\gamma_0^2|S|^2\sin^2(\theta_z/2)}{\gamma_1^2+4\gamma_0^2|S|^2\sin^2(\theta_z/2)}. \tag{87}$$

As $\mathbf{k}$ approaches either zone corner K or K', the transmission goes to zero. This is because the chains which extend through BHG are cut and shifted at the stacking fault. Curiously, the transmission coefficient T goes to unity when $\gamma_1\to 0$. Note also that along K-H and K'-H' we have $S=0$ and hence $R=1$, $T=0$. At the band edges, we have

$$R(\theta_z=0)=1,\quad R(\theta_z=\pi)=\frac{\gamma_1^2}{\gamma_1^2+4\gamma_0^2|S|^2}, \tag{88}$$

with $T=1-R$ for the transmission coefficients (Fig. 7).

C. Existence of bound states

To search for bound states, we take, for $j>0$,

$$\psi_{n=-2j}=e^{\kappa n}\chi,\quad \psi_{n=2j}=\beta e^{-\kappa n}\phi, \tag{89}$$

$$\psi_{n=-2j+1}=e^{\kappa n}\phi,\quad \psi_{n=2j+1}=\beta e^{-\kappa n}\chi, \tag{90}$$

and solve for κ, β, and E. At the plane $l=0$ we have

$$\psi_0=\begin{pmatrix}\chi_1\\ \beta\phi_2\end{pmatrix}. \tag{91}$$

The Schrödinger equation for $l\neq 0$ then yields

$$M\chi+2\gamma_1\cosh(\kappa)\Sigma^+\phi=0, \tag{92}$$

$$M\phi+2\gamma_1\cosh(\kappa)\Sigma^-\chi=0. \tag{93}$$

This yields

$$E=-\mu\gamma_1\cosh(\kappa)-\mu'\sqrt{\gamma_1^2\cosh^2(\kappa)+\gamma_0^2|S|^2}, \tag{94}$$

where once again $\mu=\pm 1$ and $\mu'=\pm 1$. Again we have

$$\phi=\begin{pmatrix}-\gamma_0 S\\ E\end{pmatrix},\quad \chi=\mu\begin{pmatrix}E\\ -\gamma_0 S^*\end{pmatrix}. \tag{95}$$

At $l=0$ we again have

$$M\psi_0+\gamma_1\Sigma^+\psi_{-1}+\gamma_1\Sigma^-\psi_{+1}=0, \tag{96}$$

which here yields

$$\begin{pmatrix}E & \gamma_0 S\\ \gamma_0 S^* & E\end{pmatrix}\begin{pmatrix}\mu\\ \beta\end{pmatrix}+\gamma_1 e^{-\kappa}\begin{pmatrix}1\\ \mu\beta\end{pmatrix}=0. \tag{97}$$

This yields two equations for β, which may be written as

$$\beta=-\frac{\mu E+\gamma_1 e^{-\kappa}}{\gamma_0 S}=-\frac{\gamma_0 S^*}{\mu E+\gamma_1 e^{-\kappa}}. \tag{98}$$

This fixes the energy at

$$E=-\mu\gamma_1 e^{-\kappa}\pm\gamma_0|S|. \tag{99}$$

Thus, we have a bound state at positive energy (and a corresponding one at negative energy) for each real positive value of κ, which solves one of the four equations (for $\mu,\mu'=\pm 1$),

$$-\mu\gamma_1 e^{-\kappa}+\mu'\gamma_0|S|=-\mu\gamma_1\cosh(\kappa)+\mu'\sqrt{\gamma_1^2\cosh^2(\kappa)+\gamma_0^2|S|^2}. \tag{100}$$

We assume $\gamma_0>0$. In the SWMC analysis,[3] one has $\gamma_1\approx -390$ meV and $\gamma_0\approx 3.2$ eV. The vertical hopping is negative due to the sign of the overlap of p_z orbitals on consecutive layers. In order to have a bound-state solution, we must have $\mu\mu'=\mathrm{sgn}(\gamma_1)$, resulting in

$$\sqrt{\gamma_1^2\cosh^2(\kappa)+\gamma_0^2|S|^2}-\gamma_0|S|=|\gamma_1|\sinh(\kappa). \tag{101}$$

The solution of which is

$$\sinh(\kappa)=\frac{|\gamma_1|}{2\gamma_0|S|}\equiv u. \tag{102}$$

Thus, there are two bound states for all $\mathbf{k}$ in the Brillouin zone, one at positive energy, corresponding to the choices $\mu=\mu'=\mathrm{sgn}(\gamma_1)$, and one at negative energy, corresponding to the choices $\mu=\mu'=-\mathrm{sgn}(\gamma_1)$. Solving for κ, we have

$$e^{\pm\kappa} = \pm u + \sqrt{1+u^2}. \tag{103}$$

The bound-state energy may now be written as

$$E_B = |\gamma_1|\left(u + \frac{1}{2u} - \sqrt{1+u^2}\right) \tag{104}$$

$$= \frac{\gamma_0^3|S|^3}{\gamma_1^2} + \mathcal{O}(u^{-5}), \tag{105}$$

where the expansion in the second line is for large u, i.e., $\gamma_0|S| \ll |\gamma_1|$. Note that the bound state disperses as $|\mathbf{k}|^3$. Recall for Bernal graphite that the dispersion is linear in $|\mathbf{k}|$ in the vicinity of H and quadratic elsewhere along the K-H spine. The length scale associated with the bound state is κ^{-1}. For $u\to\infty$, $\kappa^{-1}\sim 1/\ln(2u)$.

Since the spectrum, including bound states, is particle-hole symmetric, we may without loss of generality limit our attention to $E\geq 0$ states. The continuum bands, for fixed $\mathbf{k}$, range over energies

$$-|\gamma_1| + \sqrt{\gamma_1^2+\gamma_0^2|S|^2} \leq E_{\mathbf{k}}^{(3)} \leq \gamma_0|S|, \tag{106}$$

$$\gamma_0|S| \leq E_{\mathbf{k}}^{(4)} \leq |\gamma_1| + \sqrt{\gamma_1^2+\gamma_0^2|S|^2}. \tag{107}$$

The bound state we have analyzed lives just below the bottom of the $E_{\mathbf{k}}^{(3)}$ band. The binding energy is $\Delta = E_{\mathrm{min}}^{(3)} - E_B$ and is given by

$$\frac{\Delta(u)}{|\gamma_1|} = \frac{1}{2u}\left(\sqrt{1+4u^2}-1\right) + \sqrt{1+u^2} - 1 - u. \tag{108}$$

In Fig. 8 we plot the bound-state spectrum for the case $|\gamma_1|/\gamma_0=0.1$ for small values of $|S|$, i.e., close to the zone corners, where u is large. At the zone center, $|S|=3$ is maximized and u achieves its minimum value; for reference, $u_{\mathrm{SWMC}}=0.020\,57$. The binding energy vanishes in both the $u\to 0$ and $u\to\infty$ limits, as shown in Fig. 9. The maximum of Δ occurs for $u=1$, where $\Delta/|\gamma_1|=0.032\,25$, corresponding to a binding energy of approximately 13 meV. In the Appendix, we compute the bound-state spectrum for the full SWMC model.

V. FINITE B CASE

To obtain the Landau levels, we expand about the Dirac points, following the method described in Sec. II A. We have $S_{\mathbf{K}+\mathcal{B}/\hbar} = -\epsilon b$, with ϵ given in Eq. (26). At $B=10$ T one has $\epsilon=0.0371$. With $\gamma_1=0.39$ eV and $\gamma_0=3.16$ eV, we have $r=0.123$ and $\epsilon/r=\sqrt{B/B_1}$ where $B_1=110.8$ T. For physical fields, then, we have $\epsilon\lesssim r$. Note that one can also write

$$\epsilon\gamma_0 = \frac{\sqrt{2}\hbar v_F}{\ell_B}, \tag{109}$$

where $v_F=\sqrt{3}\gamma_0 a/2\hbar$ is the Fermi velocity ($a=2.46$ Å is the lattice spacing in the hexagonal planes) and $\ell_B=\hbar c/eB$ is the magnetic length.

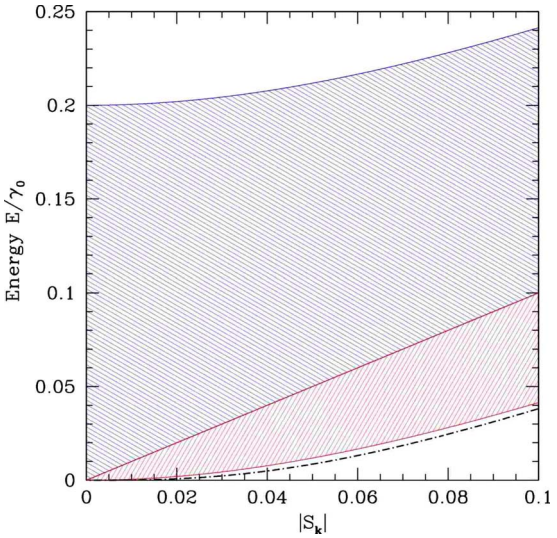

FIG. 8. (Color online) Energy bands and bound-state dispersion for $\gamma_1=0.1\gamma_0$ for small values of $|S|$. The bulk bands $E_{\mathbf{k}}^{(3,4)}$ are depicted by the red and blue hatched regions, respectively. The bound state is the thick black dot-dash curve.

A. Bernal stacking and Landau levels

We define the operator-valued matrix

$$\hat{M} = \begin{pmatrix} E & \epsilon\gamma_0 b \\ \epsilon\gamma_0 b^\dagger & E \end{pmatrix}. \tag{110}$$

For perfect Bernal stacking, we have

$$\hat{M}\psi_{2j} + \gamma_1\Sigma^+(\psi_{2j-1}+\psi_{2j+1}) = 0, \tag{111}$$

$$\hat{M}\psi_{2j+1} + \gamma_1\Sigma^-(\psi_{2j}+\psi_{2j+2}) = 0. \tag{112}$$

We now write the wave function in terms of right and left moving components,

$$\psi_{2j} = \left(Ie^{iqj} + O'e^{-iqj}\right)\begin{pmatrix} \alpha|n\rangle \\ \beta|n+1\rangle \end{pmatrix}, \tag{113}$$

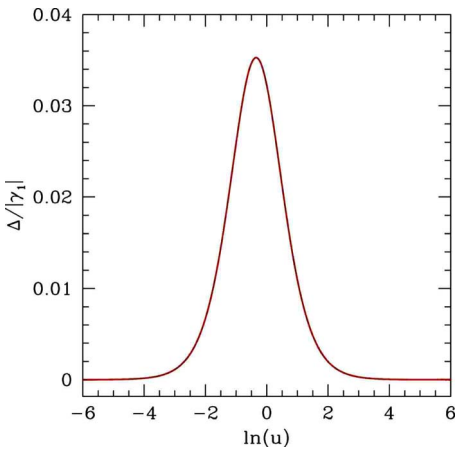

FIG. 9. (Color online) Binding energy of the bound state versus $\ln(u)$, where $u=|\gamma_1/2\gamma_0 S|$.

$$\psi_{2j+1} = (Ie^{iq(j+1/2)} + O'e^{-iq(j+1/2)})\begin{pmatrix} x|n-1\rangle \\ y|n\rangle \end{pmatrix}, \quad (114)$$

where we assume $n>0$. We therefore have

$$M_n\begin{pmatrix} x \\ y \end{pmatrix} + 2\gamma_1 \cos(q/2)\Sigma^-\begin{pmatrix} \alpha \\ \beta \end{pmatrix} = 0, \quad (115)$$

$$M_{n+1}\begin{pmatrix} \alpha \\ \beta \end{pmatrix} + 2\gamma_1 \cos(q_L/2)\Sigma^+\begin{pmatrix} x \\ y \end{pmatrix} = 0, \quad (116)$$

where

$$M_n \equiv \begin{pmatrix} E & \sqrt{n}\epsilon\gamma_0 \\ \sqrt{n}\epsilon\gamma_0 & E \end{pmatrix}. \quad (117)$$

This leads to

$$P_n(E) = \det[M_{n+1} - 4\gamma_1^2 \cos^2(q/2)\Sigma^+ M_n^{-1}\Sigma^-]$$
$$= E^2 - (n+1)\epsilon^2\gamma_0^2 - \frac{4\gamma_1^2 E^2 \cos^2(q/2)}{E^2 - n\epsilon^2\gamma_0^2}. \quad (118)$$

Setting $P_n(E)=0$ yields the spectrum $E=E_n(q)$ of Bernal hexagonal graphite,

where $r=\gamma_1/\gamma_0$. Expanding for small ϵ/r, we have

$$E_{n,-} \in \left[\sqrt{n(n+1)}\frac{\epsilon^2}{2r}, \epsilon\sqrt{n}\right], \quad (120)$$

$$E_{n,+} \in \left[\sqrt{n+1}\ \epsilon, 2r + \left(n+\frac{1}{2}\right)\frac{\epsilon^2}{2r} + \cdots\right]. \quad (121)$$

B. Zero modes

The case $n=0$ must be considered separately. Consider the wave function

$$\psi_{2j} = \begin{pmatrix} 0 \\ \beta|0\rangle \end{pmatrix}\delta_{j,J}, \quad \psi_{2j+1} = \begin{pmatrix} 0 \\ 0 \end{pmatrix}. \quad (122)$$

This is an $E=0$ eigenstate for any J. It describes a state localized on a single plane.

We can find more solutions by writing

$$\psi_{2j} = \begin{pmatrix} \alpha|0\rangle \\ \beta|1\rangle \end{pmatrix}e^{iqj}, \quad (123)$$

$$\psi_{2j+1} = \begin{pmatrix} 0 \\ y|0\rangle \end{pmatrix}e^{iq(j+1/2)}. \quad (124)$$

The Schrödinger equation then requires

$$\begin{pmatrix} E & \epsilon\gamma_0 \\ \epsilon\gamma_0 & E \end{pmatrix}\begin{pmatrix} \alpha \\ \beta \end{pmatrix} + 2\gamma_1 \cos(q/2)\begin{pmatrix} y \\ 0 \end{pmatrix} = 0 \quad (125)$$

on even planes and

$$E\begin{pmatrix} 0 \\ y \end{pmatrix} + 2\gamma_1 \cos(q/2)\begin{pmatrix} 0 \\ \alpha \end{pmatrix} = 0 \quad (126)$$

on odd planes. Thus, we have three equations for the remaining three eigenvalues:

$$0 = E\alpha + \epsilon\gamma_0\beta + 2\gamma_1 \cos(q/2)y, \quad (127)$$

$$0 = E\beta + \epsilon\gamma_0\alpha, \quad (128)$$

$$0 = Ey + 2\gamma_1 \cos(q/2)\alpha. \quad (129)$$

We immediately see that $E=0$ is an eigenvalue, with eigenvector

$$\begin{pmatrix} \alpha \\ \beta \\ y \end{pmatrix} = \begin{pmatrix} 0 \\ -2\gamma_1 \cos(q/2) \\ \epsilon\gamma_0 \end{pmatrix}. \quad (130)$$

If we Fourier transform this solution, multiplying by $e^{-iq(J+1/2)}$ and summing over q, we find a purely localized state, with

$$\psi_{2J} = -\gamma_1\begin{pmatrix} 0 \\ |1\rangle \end{pmatrix}, \quad (131)$$

$$\psi_{2J+1} = \epsilon\gamma_0\begin{pmatrix} 0 \\ |0\rangle \end{pmatrix}, \quad (132)$$

$$\psi_{2J+2} = -\gamma_1\begin{pmatrix} 0 \\ |1\rangle \end{pmatrix}, \quad (133)$$

with all other $\psi_n=0$. This zero mode is localized on three layers. The remaining two solutions are easily found to be

$$\begin{pmatrix} \alpha \\ \beta \\ y \end{pmatrix} = \begin{pmatrix} E \\ -\epsilon\gamma_0 \\ -2\gamma_1 \cos(q/2) \end{pmatrix}, \quad (134)$$

with $E=E_{0,\pm} \equiv \pm\sqrt{\epsilon^2\gamma_0^2 + 4\gamma_1^2 \cos^2(q/2)}$. These solutions are wavelike and disperse with q.

C. Stacking fault

For the system with a single-step stacking fault, the situation is as depicted in Fig. 11. We then swap the notation for even and odd planes on the right half of the system (layer indices $l>0$) with respect to Eq. (114) and introduce wave vectors q_L and q_R for the left and right half systems. We must then match the energies on left and right sides of the fault as follows:

$$E_n(q_L) = E_{n+1}(q_R). \quad (135)$$

To identify the bound states, we write the wave function for $l>0$ as

$$\psi_{2j-1} = \begin{pmatrix} \alpha_j|n+1\rangle \\ \beta_j|n+2\rangle \end{pmatrix}, \quad \psi_{2j} = \begin{pmatrix} x_j|n\rangle \\ y_j|n+1\rangle \end{pmatrix} \quad (136)$$

and for $l<0$ as

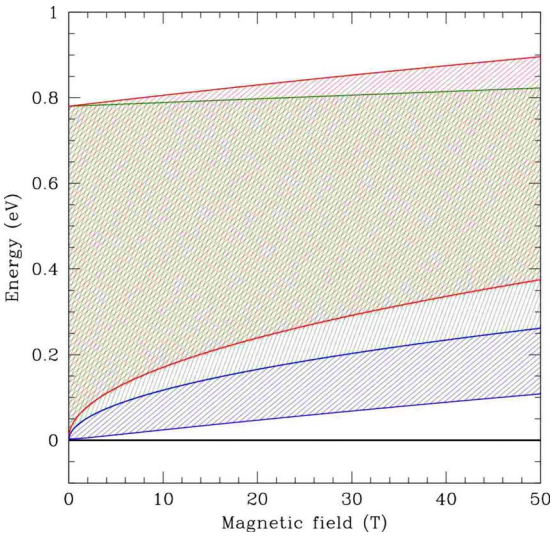

FIG. 10. (Color online) Landau levels in graphite. Subbands $E_{n=1,+}$ (red), $E_{n=1,-}$ (blue), and $E_{n=0,+}$ (green) are shown. The zero modes are shown in black.

$$\psi_{-(2j-1)} = \begin{pmatrix} \bar{\alpha}_j|n-1\rangle \\ \bar{\beta}_j|n\rangle \end{pmatrix}, \quad \psi_{-2j} = \begin{pmatrix} \bar{x}_j|n\rangle \\ \bar{y}_j|n+1\rangle \end{pmatrix}. \tag{137}$$

At $l=0$ we write

$$\psi_0 = \begin{pmatrix} \bar{x}_0|n\rangle \\ y_0|n+1\rangle \end{pmatrix}. \tag{138}$$

The Schrödinger equation, evaluated for both even and odd planes with $l>0$ and $l<0$, now gives eight relations among the eight sets of coefficients $\{\alpha_j,\beta_j,x_j,y_j,\bar{\alpha}_j,\bar{\beta}_j,\bar{x}_j,\bar{y}_j\}$ expressible as

$$\begin{pmatrix} E & \sqrt{n+1}\epsilon\gamma_0 \\ \sqrt{n+1}\epsilon\gamma_0 & E \end{pmatrix}\begin{pmatrix} x_j \\ y_j \end{pmatrix} + \gamma_1\begin{pmatrix} 0 \\ \alpha_j+\alpha_{j+1} \end{pmatrix} = 0 \tag{139}$$

$$\begin{pmatrix} E & \sqrt{n+2}\epsilon\gamma_0 \\ \sqrt{n+2}\epsilon\gamma_0 & E \end{pmatrix}\begin{pmatrix} \alpha_j \\ \beta_j \end{pmatrix} + \gamma_1\begin{pmatrix} y_{j-1}+y_j \\ 0 \end{pmatrix} = 0, \tag{140}$$

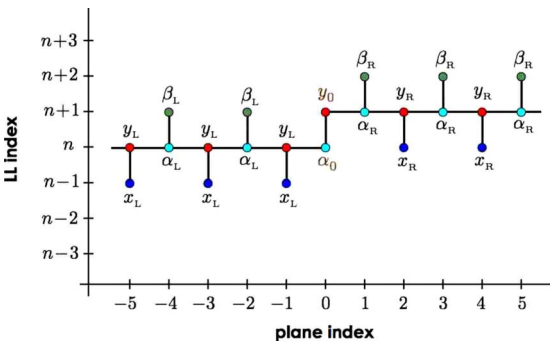

FIG. 11. (Color online) Landau-level indices for scattering at a stacking fault in Bernal graphite.

$$\begin{pmatrix} E & \sqrt{n+1}\epsilon\gamma_0 \\ \sqrt{n+1}\epsilon\gamma_0 & E \end{pmatrix}\begin{pmatrix} \bar{x}_j \\ \bar{y}_j \end{pmatrix} + \gamma_1\begin{pmatrix} \bar{\beta}_j+\bar{\beta}_{j+1} \\ 0 \end{pmatrix} = 0, \tag{141}$$

$$\begin{pmatrix} E & \sqrt{n}\epsilon\gamma_0 \\ \sqrt{n}\epsilon\gamma_0 & E \end{pmatrix}\begin{pmatrix} \bar{\alpha}_j \\ \bar{\beta}_j \end{pmatrix} + \gamma_1\begin{pmatrix} 0 \\ \bar{x}_{j-1}+\bar{x}_j \end{pmatrix} = 0. \tag{142}$$

We can use these equations to eliminate the four sets of coefficients $\{\beta_j,x_j,\bar{\alpha}_j,\bar{y}_j\}$,

$$\beta_j = -\sqrt{n+2}\epsilon\gamma_0 E^{-1}\alpha_j, \tag{143}$$

$$\bar{y}_j = -\sqrt{n+1}\epsilon\gamma_0 E^{-1}\bar{x}_j, \tag{144}$$

$$x_j = -\sqrt{n+1}\epsilon\gamma_0 E^{-1} y_j \tag{145}$$

$$\bar{\alpha}_j = -\sqrt{n}\epsilon\gamma_0 E^{-1}\bar{\beta}_j. \tag{146}$$

We then obtain

$$0 = R_{n+1}(E)y_j + \alpha_j + \alpha_{j+1}, \tag{147}$$

$$0 = R_{n+2}(E)\alpha_j + y_{j-1} + y_j, \tag{148}$$

$$0 = R_{n+1}(E)\bar{x}_j + \bar{\beta}_j + \bar{\beta}_{j+1}, \tag{149}$$

$$0 = R_n(E)\bar{\beta}_j + \bar{x}_{j-1} + \bar{x}_j, \tag{150}$$

where

$$R_n(E) \equiv \frac{E^2 - E_n^2}{E\gamma_1} \tag{151}$$

with $E_n^2 \equiv n\epsilon^2\gamma_0^2$. We then have

$$\begin{pmatrix} \alpha_{j+1} \\ y_j \end{pmatrix} = (K_{n+1})^j\begin{pmatrix} \alpha_1 \\ y_0 \end{pmatrix} \tag{152}$$

and

$$\begin{pmatrix} \bar{\beta}_{j+1} \\ \bar{x}_j \end{pmatrix} = (K_n)^j\begin{pmatrix} \bar{\beta}_1 \\ \bar{x}_0 \end{pmatrix}, \tag{153}$$

where

$$K_n(E) = \begin{pmatrix} R_n(E)R_{n+1}(E) - 1 & R_n(E) \\ -R_{n+1}(E) & -1 \end{pmatrix}. \tag{154}$$

Note that $\det K_n(E)=1$ and that the characteristic polynomial $\det(\lambda - K_n)$ is real for real λ. It is easy to see that the eigenvalues of $K_n(E)$ form a complex-conjugate pair $e^{\pm i\theta}$ if the energy E satisfies the condition the condition $|\mathrm{Tr}\, K_n(E)| \leq 2$ or

$$0 \leq R_n(E)R_{n+1}(E) \leq 4. \tag{155}$$

This is the condition that E lies within one of four energy bands. The roots of $R_n(E)R_{n+1}(E)=0$ lie at $E^2=E_n^2$ and $E^2=E_{n+1}^2$, while the roots of $R_n(E)R_{n+1}(E)=4$ lie at $E^2=E_{n,-}^2$ and $E^2=E_{n+1,+}^2$, where

$$E^2_{n,\pm} = \left(n+\tfrac{1}{2}\right)\epsilon^2\gamma_0^2 + 2\gamma_1^2 \pm \sqrt{4\gamma_1^4 + (4n+2)\epsilon^2\gamma_0^2\gamma_1^2 + \left(\tfrac{1}{2}\right)\epsilon^4\gamma_0^4}. \tag{156}$$

The bands (see Fig. 10) are then given by

$$E^2_{n,-} \le E^2 \le E^2_n, \quad E^2_{n+1} \le E^2 \le E^2_{n,+}. \tag{157}$$

In the limit $\sigma \equiv \epsilon^2\gamma_0^2/\gamma_1^2 \ll 1$, we can expand and write

$$E^2_{n,-} \simeq n(n+1)\frac{\epsilon^4\gamma_0^4}{4\gamma_1^2}, \tag{158}$$

$$E_{n,+} \simeq 4\gamma_1^2 + (2n+1)\epsilon^2\gamma_0^2. \tag{159}$$

At plane $n=0$ the Schrödinger equation yields

$$\begin{pmatrix} \gamma_1 & E \\ 0 & \sqrt{n+1}\,\epsilon\gamma_0 \end{pmatrix}\begin{pmatrix} \bar{\beta}_1 \\ \bar{x}_0 \end{pmatrix} + \begin{pmatrix} 0 & \sqrt{n+1}\,\epsilon\gamma_0 \\ \gamma_1 & E \end{pmatrix}\begin{pmatrix} \alpha_1 \\ y_0 \end{pmatrix} = 0. \tag{160}$$

D. Scattering matrix

If both $|\mathrm{Tr}\, K_n(E)| \le 2$ and $|\mathrm{Tr}\, K_{n+1}(E)| \le 2$, then we can write

$$\begin{pmatrix} \bar{\beta}_1 \\ \bar{x}_0 \end{pmatrix} = I\Psi^{(n)}_- + O'\Psi^{(n)}_+ \tag{161}$$

and

$$\begin{pmatrix} \alpha_1 \\ y_0 \end{pmatrix} = I'\Psi^{(n+1)}_- + O\Psi^{(n+1)}_+, \tag{162}$$

where

$$K_n(E)\Psi^{(n)}_\pm = e^{\pm i\theta_n}\Psi^{(n)}_\pm. \tag{163}$$

Then we have

$$\begin{pmatrix} \bar{\beta}_{j+1} \\ \bar{x}_j \end{pmatrix} = Ie^{-ij\theta_n}\Psi^{(n)}_- + O'e^{ij\theta_n}\Psi^{(n)}_+ \tag{164}$$

$$\begin{pmatrix} \alpha_{j+1} \\ y_j \end{pmatrix} = I'e^{-ij\theta_{n+1}}\Psi^{(n+1)}_- + Oe^{ij\theta_{n+1}}\Psi^{(n+1)}_+. \tag{165}$$

The $\mathcal{S}$ matrix, which relates incoming to outgoing flux amplitudes, is then obtained from Eqs. (160)–(162), upon replacing $I \to v_L^{1/2}\mathcal{I}$, $O \to \mathcal{O}'v_L^{1/2}$, $I' \to v_R^{1/2}\mathcal{I}$, and $O \to \mathcal{O}v_R^{1/2}$, where $v_L = \partial E_n(q_L)/\partial q_L$ and $v_R = \partial E_{n+1}(q_R)/\partial q_R$.

E. Bound states

If a state is evanescent on both sides of the stacking fault, we must have that both $|\mathrm{Tr}\, K_n(E)| > 2$ and $|\mathrm{Tr}\, K_{n+1}(E)| > 2$. The eigenvalues of $K_n(E)$ are given by

$$\Lambda_{n,\pm} = \tfrac{1}{2}\tau_n \pm \tfrac{1}{2}\sqrt{\tau_n^2 - 4}, \tag{166}$$

where

$$\tau_n(E) \equiv \mathrm{Tr}\, K_n(E) = R_n(E)R_{n+1}(E) - 2. \tag{167}$$

In order that the solution in Eq. (153) not blow up for $n \to \pm\infty$, we must require that $\binom{\alpha_1}{y_0}$ and $\binom{\bar{\beta}_1}{\bar{x}_0}$ have no weight in the $|\Lambda| > 1$ eigenspaces for $K_n(E)$ and $K_{n+1}(E)$, respectively. This means

$$R_{n+2}(E)\alpha_1 + y_0 = -\Lambda^<_{n+1}y_0, \tag{168}$$

$$R_{n+1}(E)\bar{\beta}_1 + \bar{x}_0 = -\Lambda^<_n\bar{x}_0, \tag{169}$$

where $|\Lambda^<| < 1$. When we combine these equations with those in Eq. (160), we obtain

$$\mathcal{M}\begin{pmatrix} \alpha_1 \\ y_0 \\ \bar{\beta}_1 \\ \bar{x}_0 \end{pmatrix} = 0, \tag{170}$$

where

$$\mathcal{M} = \begin{pmatrix} R_{n+2} & 1+\Lambda^<_{n+1} & 0 & 0 \\ \gamma_1 & E & 0 & \sqrt{n+1}\,\epsilon\gamma_0 \\ 0 & 0 & R_{n+1} & 1+\Lambda^<_n \\ 0 & \sqrt{n+1}\,\epsilon\gamma_0 & \gamma_1 & E \end{pmatrix}. \tag{171}$$

A solution requires $D(E) = \det \mathcal{M}(E) = 0$. We have

$$D(E) = [ER_{n+2} - \gamma_1(1+\Lambda^<_{n+1})][ER_{n+1} - \gamma_1(1+\Lambda^<_n)] - (n+1)\epsilon^2\gamma_0^2R_{n+1}R_{n+2}. \tag{172}$$

Let us look for a bound state with energy E which is parametrically (in σ) smaller than both γ_1 and $\epsilon\gamma_0$. Then $R_n(E) \simeq -E_n^2/E\gamma_1$, from which we obtain $\Lambda^<_n \simeq (R_nR_{n+1})^{-1}$. Then find

$$D(E) \approx \gamma_1^2 - (n+1)^2(n+2)\frac{\epsilon^6\gamma_0^6}{\gamma_1^2E^2}. \tag{173}$$

Setting $D(E)=0$ yields the bound-state energy,

$$E^2 = (n+1)^2(n+2)\frac{\epsilon^6\gamma_0^6}{\gamma_1^4}. \tag{174}$$

Thus, the bound-state energy is proportional to $|B|^{3/2}$. In Fig. 12, we plot the lowest ten bound state energies versus magnetic field.

VI. SURFACE SPECTROSCOPY OF BURIED STACKING FAULTS

Our previous results for the transmission through a stacking defect suggest that these defects are very effective in decoupling graphene stacks. We analyze now the density of states at a graphite surface in the presence of a stacking defect a few layers below the surface. The stacking sequence is $(AB)_{N/2}CBCB\cdots$. The number of layers between the surface and the defect is N.

The system can be separated into a perfect semi-infinite graphite sample coupled to the defect layer and N layers

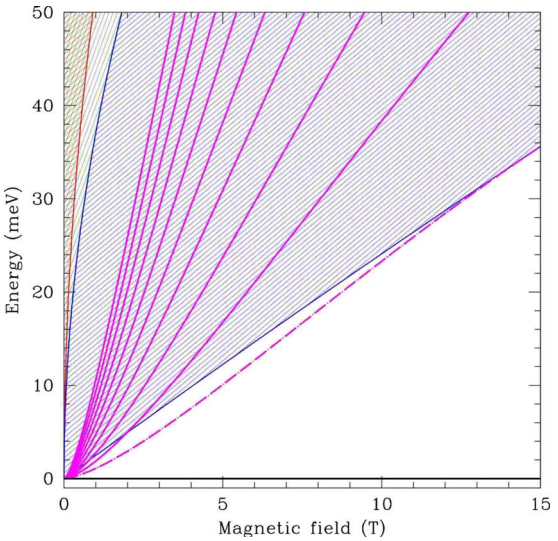

FIG. 12. (Color online) Bulk energy bands (shaded and hatched regions) and bound states (magenta curves) versus magnetic field for $\gamma_0=3.16$ eV and $\gamma_1=-0.39$ eV (tight binding; nearest-neighbor hopping only). The lowest energy bound state merges into the band continuum at $B\approx 15$ T. The other bound states remain sharp over the energy range shown and do not mix with the lowest bulk band.

between the defect and the surface. We will only include the parameters γ_0 and γ_1. The semi-infinite portion can be integrated out. The site of the defect layer connected to it acquires a self-energy

$$\Sigma_0(\omega)=\frac{2\gamma_1^2}{\left(\omega-\frac{|\gamma_0 S|^2}{\omega}\right)-\sqrt{\left(\omega-\frac{|\gamma_0 S|^2}{\omega}\right)^2-4\gamma_1^2}}. \tag{175}$$

We now integrate out this site, leading to the self-energy

$$\Sigma_1(\omega)=\frac{|\gamma_0 S|^2}{\omega-\Sigma_0(\omega)}. \tag{176}$$

The procedure can be iterated leading to other self-energies for sites $2,3,\ldots,N$, resulting in the hierarchy

$$\Sigma_{i+1}(\omega)=\frac{|\gamma_0 S|^2}{\omega}+\frac{\gamma_1^2}{\omega-\Sigma_i(\omega)} \tag{177}$$

The Green's functions at the two inequivalent sites of the surface layer (N) are

$$G_u^N(\omega)=\frac{1}{\omega-\frac{|\gamma_0 S|^2}{\omega}-\frac{\gamma_1^2}{\omega-\Sigma_{N-1}(\omega)}} \tag{178}$$

and

$$G_v^N(\omega)=\frac{1}{\omega-\frac{|\gamma_0 S|^2}{\omega-\frac{\gamma_1^2}{\omega-\Sigma_{N-1}(\omega)}}}. \tag{179}$$

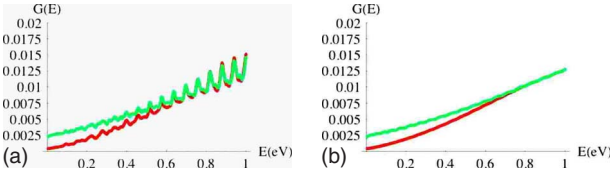

FIG. 13. (Color online) Left: Density of states for the two inequivalent sites of a graphite surface with a stacking defect 20 layers below the surface. Triangles (red) give the density of states at the site with a nearest neighbor in the layer below. Squares (green) give the density of states at the site without nearest neighbors in the layer below. Right: as in the left panel, with a defect 100 layers below the surface.

We show in Fig. 13 the surface density of states when such a defect lies twenty and hundred layers below the surface obtained by integrating the imaginary part of the Green's functions in Eq. (179) over the in-plane component $\mathbf{k}_\parallel$ of the wave vector.

The density of states show a number of resonances, which are smoothed out when the number of layers between the defect and the surface is large. For $N\gg 1$, we recover the analytical results in Ref. 15. These results are consistent with the analysis in Secs. I–V, which show that the transmission through the defect is strongly suppressed. The layers between the defect and the surface become effectively decoupled from the bulk of the system.

The previous analysis can be extended to the study of Landau levels in a magnetic field. As discussed earlier, the hoppings within the layers depend now on the Landau-level index n instead of on $\mathbf{k}_\parallel$. The n dependence of the hoppings in the two layers within the unit cell is different. Because of this, the self-energy obtained by integrating out the perfect semi-infinite region leads to a more complicated expression than those in Eq. (175). Within the region between the defect and the surface the successive self-energies have a twofold periodicity

$$\Sigma_i(\omega)=\frac{nv_F^2\ell_B^{-2}}{\omega}+\frac{\gamma_1^2}{\omega-\Sigma_{i-1}(\omega)}, \tag{180}$$

$$\Sigma_{i+1}(\omega)=\frac{(n-1)v_F^2\ell_B^{-2}}{\omega}+\frac{\gamma_1^2}{\omega-\Sigma_i(\omega)}. \tag{181}$$

The resulting densities of states for Landau-level index $n=2$ and two magnetic fields, $B=1$ T and $B=10$ T, are shown in Fig. 14.

We show finally in Fig. 15 the dependence of the peaks in the surface density of states on the magnetic field. As before, there is a stacking defects ten layers below the surface. In agreement with experiments,[16–18] there are peaks which scale as $\sqrt{B}$ and peaks which scale as B.

VII. DISCUSSION

We have analyzed the appearance of two-dimensional features in bulk graphite. We show that deviations from the Bernal stacking order are very effective in inducing two-dimensional behavior. An ordered array of graphene layers

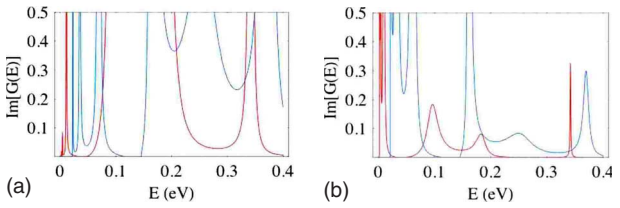

FIG. 14. (Color online) Surface density of states for a semi-infinite stack with a defect ten layers below the surface. The Landau-level index is $n=2$, and the fields studied are $B=1$ T (red) and $B=10$ T (blue). Left: Sublattice with a nearest neighbor in the contiguous layer. Right: Sublattice without a neighbor in the contiguous layer.

with the rhombohedral stacking order leads to isolated Landau levels and to quantized quantum Hall plateaus at moderate magnetic fields in doped systems. We found that the gap between Landau-level subbands of indices n and $n+1$ opens at a field $B_{c,n}$ with $B_{c,n=0} \equiv B_0 = 0.123$ T and $B_{c,n} \sim 4nB_0$ for large n. By contrast, in Bernal graphite, the first gap is predicted to open at fields on the order of 10 T,[5] and the second gap opens only at enormous field on the order of 1000 T.

We have also considered the simplest stacking defect in Bernal graphite, which has locally a rhombohedral arrangement. These defects are expected to be common in many graphite samples, and concentrations up to 10% have been reported.[2,21,22] These defects are very effective in decoupling the electronic states on either side. They also give rise to a two-dimensional band of electronic states localized in the vicinity of the defect. Within a nearest-neighbor tight-binding model for the π band of graphite, with in-plane hopping $\gamma_0 = 3.16$ eV and interplane hopping $\gamma_1 = 0.39$ eV, we found a maximum binding energy of approximately 13 meV for states rather close to the corners in the basal Brillouin zone. When the full SWMC model is taken into account,[3] we obtain a maximum binding energy of almost 40 meV for electron states and 20 meV for hole states; the binding energy is significant only along the zone faces.

What are the implications of our work for magnetotransport in graphite with stacking faults? To describe the physics, it is helpful to keep in mind the bound-state Landau-level structure of Fig. 12. First, suppose the graphite is undoped. In this case, the Fermi level remains pinned within the central $n=0$ Landau levels. With only nearest-neighbor hoppings, there are two flat bands (i.e., which do not disperse as a function of k_z) at $E=0$ associated with each zone corner in the basal Brillouin zone. Taking into account the weak second-neighbor plane hoppings γ_2 and γ_5, these bands disperse and acquire a width of about 40 meV. For the full SWMC model, due to the breaking of electron-hole symmetry, the Fermi level can drift within these central Landau subbands even if the system is at electroneutrality. As shown by Yoshioka and Fukuyama,[23] due to interaction effects one then expects a charge-density wave (CDW) at sufficiently high fields. Anomalies in the observed magnetotransport data corresponding to this CDW transition have indeed been observed.[24] The presence of stacking faults, which produce bound states away from the central Landau levels, should not affect this picture.

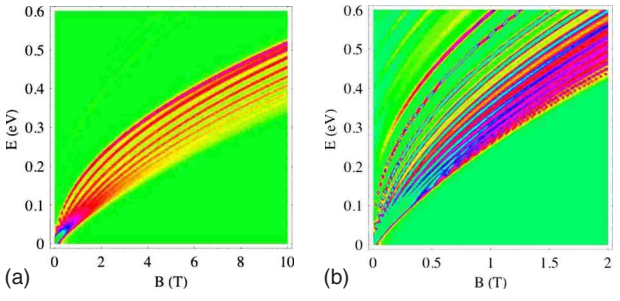

FIG. 15. (Color online) Surface density of states at the sublattice without a nearest neighbor in the next layer. The system has a stacking fault of the type described in the text ten layers from the surface. Top: $n=2$. Bottom: $n=10$.

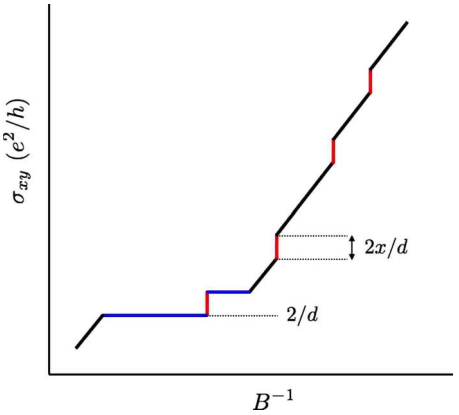

FIG. 16. (Color online) Sketch of the expected behavior of the Hall conductivity in the quantum limit for a lightly doped system. The leftmost plateau is a bulk effect related to the Landau levels of Bernal graphite (Ref. 5). The size of the other jumps depends on the concentration x of stacking defects. The continuum bands of Landau levels lead to a monotonically varying conductivity.

However, if the graphite is lightly doped, a different picture emerges.[5] In this case, the central Landau levels become filled at a field $B^* = \frac{1}{2} nd\phi_0$, where n is the bulk carrier density and d is the interplane separation (i.e., the c-axis lattice constant is $2d$ due to Bernal stacking). For fields $B < B^*$, the central Landau bands are filled and the Hall conductivity should be quantized at a value $2e^2/hd$.[5] As B is decreased further, the Fermi level crosses the bound-state energy. The bound-state Landau levels (one for each spin value and inequivalent zone corner) then makes a contribution to σ_{xy}, of magnitude $\Delta\sigma_{xy}^{\text{fault}} = 2xe^2/hd$, as shown in the sketch in Fig. 16, where x is the concentration of stacking faults. Upon further reducing B, the Fermi level enters into the first bulk band and σ_{xy} begins to rise continuously. As E_F crosses other bound-state Landau levels, additional small jumps of $\Delta\sigma_{xy}^{\text{fault}} = 2xe^2/hd$ should appear. At a finite concentration x of stacking faults, the bound states will themselves form a band, and the small jumps will no longer have infinite slope. The scenario discussed here shows how anomalous features could occur in the high-field magnetotransport of doped graphite; however, we cannot find any obvious connection between our work and the observations of Kempa *et al.*[14]

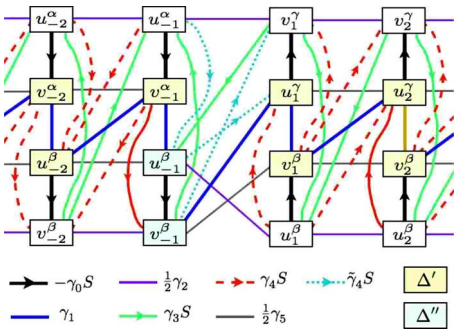

FIG. 17. (Color online) SWMC couplings for a stacking defect in Bernal graphite showing more clearly the four sublattice structure on either side of the defect.

Stacking defects below a graphite surface decouple the surface region from the bulk, leading to quasi-two-dimensional behavior, with localized Landau levels. We have shown how such buried defects leave a signature which can be measured by surface spectroscopy.

Note that the quasi-two-dimensional features in bulk graphite analyzed here have been obtained for interlayer couplings in the upper range of those discussed in the literature. Lower values will further enhance these effects. Finally, our results suggest that the electronic properties of few layer graphene samples can be substantially modified by changes in the stacking order.

ACKNOWLEDGMENTS

The authors gratefully acknowledge conversations with A. Bernevig, P. Esquinazi, M. Fogler, N. García, T. Hughes, and S. Raghu. This work was supported by MEC (Spain) through Grant No. FIS2005-05478-C02-01 and CONSOLIDER Grant No. CSD2007-00010, by the Comunidad de Madrid through CITECNOMIK Grant No. CM2006-S-0505-ESP-0337, and by the EU Contract No. 12881 (NEST).

APPENDIX: FULL SWMC TREATMENT OF STACKING FAULT

We define the vectors

$$\psi_n = \begin{pmatrix} u_n^{\alpha} \\ v_n^{\alpha} \\ u_n^{\beta} \\ v_n^{\beta} \end{pmatrix} \quad (n<0), \qquad \phi_n = \begin{pmatrix} v_n^{\gamma} \\ u_n^{\gamma} \\ v_n^{\beta} \\ u_n^{\beta} \end{pmatrix} \quad (n>0). \tag{A1}$$

For a stacking defect *ABABCBCB* the SWMC couplings are depicted in Fig. 17. In fact, additional couplings must be introduced at the defect. In the bulk, sites have either zero or two c-axis neighbors, but at the stacking fault there are two sites with a single such neighbor. One expects the associated on-site energy $\Delta'' \approx \frac{1}{2}\Delta$. In addition, there are three interlayer couplings at the defect which in principle are distinct from γ_3 and γ_4 and which we denote in the figure by dotted pale blue lines, with hopping amplitude $\tilde{\gamma}_4$. For simplicity, we shall take $\Delta''=\Delta$ and $\tilde{\gamma}_4=\gamma_4$ for two of the links and $\tilde{\gamma}_4=\gamma_3$ for the other link. For details, see the definition of the F matrix below.

Let each pair of layers be indexed by a nonzero integer n. From the figures, we can read off the Schrödinger equations

$$M\psi_{n-1} + K\psi_n + M^{\dagger}\psi_{n+1} = 0 \quad (n<-1), \tag{A2}$$

$$M^{*}\phi_{n-1} + K^{*}\phi_n + M^{t}\phi_{n+1} = 0 \quad (n>1), \tag{A3}$$

where, consistent with the full SWMC Hamiltonian,[3,19]

$$K = \begin{pmatrix} -E & -\gamma_0 S & \gamma_4 S & \gamma_3 S^{*} \\ -\gamma_0 S^{*} & -E+\Delta' & \gamma_1 & \gamma_4 S \\ \gamma_4 S^{*} & \gamma_1 & -E+\Delta' & -\gamma_0 S \\ \gamma_3 S & \gamma_4 S^{*} & -\gamma_0 S^{*} & -E \end{pmatrix} \tag{A4}$$

and

$$M = \begin{pmatrix} \frac{1}{2}\gamma_2 & 0 & \gamma_4 S & \gamma_3 S^{*} \\ 0 & \frac{1}{2}\gamma_5 & \gamma_1 & \gamma_4 S \\ 0 & 0 & \frac{1}{2}\gamma_5 & 0 \\ 0 & 0 & 0 & \frac{1}{2}\gamma_2 \end{pmatrix}. \tag{A5}$$

We take the following SWMC parameters from Ref. 19:

$$\gamma_0 = 3160 \text{ meV}, \quad \gamma_1 = 390 \text{ meV},$$

$$\gamma_2 = -20 \text{ meV}, \quad \gamma_3 = 315 \text{ meV},$$

$$\gamma_4 = 44 \text{ meV}, \quad \gamma_5 = 38 \text{ meV},$$

with $\Delta=-8$ meV. Here, Δ' is a combination of the original SWMC parameters,

$$\Delta' = \Delta + \gamma_5 - \gamma_2, \tag{A6}$$

hence $\Delta'=50$ meV.

At the defect, the Schrödinger equation yields

$$M\psi_{-2} + K\psi_{-1} + F^{\dagger}\phi_1 = 0, \tag{A7}$$

$$F\psi_{-1} + K^{*}\phi_1 + M^{t}\phi_2 = 0, \tag{A8}$$

where

$$F = \begin{pmatrix} \frac{1}{2}\gamma_2 & 0 & \gamma_3 S & \gamma_4 S^{*} \\ 0 & 0 & \gamma_4 S^{*} & \gamma_1 \\ 0 & 0 & 0 & \frac{1}{2}\gamma_5 \\ 0 & 0 & \frac{1}{2}\gamma_2 & 0 \end{pmatrix}. \tag{A9}$$

1. Scattering matrix and bound states

We write $\psi_n = z^n\chi$ (for $n<0$) and $\phi_n = z^{*n}\chi^{*}$ (for $n>0$). In the bulk ($|n|>0$), we then have (for both sides)

$$(z^{-1}M + K + zM^{\dagger})\chi = 0. \tag{A10}$$

In order for a solution to exist, we require

$$P(z) \equiv \det(z^{-1}M + K + zM^{\dagger}) = 0, \tag{A11}$$

which is an eighth-order equation in z. Note that $P(z)=0$ guarantees that $P(z^{*-1})=0$. It can also be shown, due to the

form of M, that $P(z)=P(z^{-1})$. Thus, the allowed values of z come in sets (z,z^*,z^{-1},z^{*-1}).

Within a bulk energy band, two of the eight z roots are unimodular and may be written as $z_1=e^{ik}$ and $z_5=e^{-ik}$ with k real. Their associated eigenvectors are $\chi_{1,5}$. Of the remaining six roots, three (z_2,z_3,z_4) each have modulus greater than unity and are thus un-normalizable on the right. The remaining three roots (z_6,z_7,z_8) each have modulus smaller than unity and are un-normalizable on the left. We keep only the normalizable solutions and write

$$n<0:\quad \psi_n=\mathcal{I}e^{ikn}\chi_1+\mathcal{O}'e^{-ikn}\chi_5+A_2z_2^n\chi_3+A_3^nz_3^n\chi_3+A_4z_4^n\chi_4, \tag{A12}$$

$$n>0:\quad \phi_n=\mathcal{I}'e^{-ikn}\chi_1^*+\mathcal{O}e^{ikn}\chi_5^*+A_6z_6^{*n}\chi_6^*+A_7z_7^{*n}\chi_7^*+A_8z_8^{*n}\chi_8^*. \tag{A13}$$

Equations (A7) and (A8) then yield eight equations in the ten unknowns $(\mathcal{I},\mathcal{O},\mathcal{I}',\mathcal{O}')$ and $(A_2,A_3,A_4,A_6,A_7,A_8)$. These then determine, for each energy E, the $\mathcal{S}$ matrix defined by the relation

$$\begin{pmatrix}\mathcal{O}\\ \mathcal{O}'\end{pmatrix}=\overbrace{\begin{pmatrix}t & r'\\ r & t'\end{pmatrix}}^{\mathcal{S}}\begin{pmatrix}\mathcal{I}\\ \mathcal{I}'\end{pmatrix}. \tag{A14}$$

If two bands overlap, then we have eigenvalues $z_{1,5}=e^{\pm ik}$ and $z_{2,6}=e^{\pm ip}$, with $|z_{3,4}|>1$ and $|z_{7,8}|<1$;

$$n<0:\quad \psi_n=\mathcal{I}e^{ikn}\chi_1+\mathcal{O}'e^{-ikn}\chi_5+\tilde{\mathcal{I}}e^{ipn}\chi_2+\tilde{\mathcal{O}}'e^{-ipn}\chi_6+A_3^nz_3^n\chi_3+A_4z_4^n\chi_4, \tag{A15}$$

$$n>0:\quad \phi_n=\mathcal{I}'e^{-ikn}\chi_1^*+\mathcal{O}e^{ikn}\chi_5^*+\tilde{\mathcal{I}}'e^{-ipn}\chi_2^*+\tilde{\mathcal{O}}e^{ipn}\chi_6^*+A_7z_7^{*n}\chi_7^*+A_8z_8^{*n}\chi_8^*. \tag{A16}$$

The S matrix is then 4×4, and we should take care to properly define it to act on *flux amplitudes*, viz.,

$$\begin{pmatrix}v_{1,k}^{1/2}\mathcal{O}\\ v_{1,k}^{1/2}\mathcal{O}'\\ v_{2,p}^{1/2}\tilde{\mathcal{O}}\\ v_{2,p}^{1/2}\tilde{\mathcal{O}}'\end{pmatrix}=\mathcal{S}\begin{pmatrix}v_{1,k}^{1/2}\mathcal{I}\\ v_{1,k}^{1/2}\mathcal{I}'\\ v_{2,p}^{1/2}\tilde{\mathcal{I}}\\ v_{2,p}^{1/2}\tilde{\mathcal{I}}'\end{pmatrix}, \tag{A17}$$

where $v_{1,k}=\partial E_1(k)/\partial k$ and $v_{2,p}=\partial E_2(p)/\partial p$. If three bands overlap, the S matrix is 6×6.

2. Bound states

When E does not lie within a bulk band, we write

$$n<0:\quad \psi_n=A_1z_1^n\chi_1+A_2z_2^n\chi_2+A_3^nz_3\chi_3+A_4z_4^n\chi_4, \tag{A18}$$

$$n>0:\quad \phi_n=A_5z_5^{*n}\chi_5^*+A_6z_6^{*n}\chi_6^*+A_7z_7^{*n}\chi_7^*+A_8z_8^{*n}\chi_8^*. \tag{A19}$$

Here, $|z_{1,2,3,4}|>1$ and $|z_{5,6,7,8}|<1$. Without loss of generality, we may assume

$$z_u^*=z_{u+4}^{-1}, \tag{A20}$$

for $u=1,2,3,4$. Equations (A7) and (A8) now give eight homogeneous equations in the eight unknowns A_{1-8}. A nontrivial solution can only exist when the corresponding determinant vanishes, which puts a single complex condition on the energy E. The solutions are the allowed bound states.

We now apply Eqs. (A7) and (A8)

$$M\psi_{-2}+K\psi_{-1}+F^\dagger\phi_1=0 \tag{A21}$$

$$F\psi_{-1}+K^*\phi_1+M^t\phi_2=0 \tag{A22}$$

to

$$\psi_n=\sum_{u=1}^{4}A_uz_u^n\chi_u,\quad \phi_n=\sum_{l=5}^{8}A_lz_l^{*n}\chi_l^* \tag{A23}$$

using

$$(z^{-1}M+K+zM^\dagger)\chi=0, \tag{A24}$$

$$(z^{*-1}M^*+K^*+z^*M^t)\chi^*=0. \tag{A25}$$

This yields

$$M^\dagger\psi_0=F^\dagger\phi_1,\quad F\psi_{-1}=M^*\phi_0, \tag{A26}$$

which, when expanded, gives

$$\sum_{u=1}^{4}A_uM^\dagger\chi_u=\sum_{l=5}^{8}A_lz_l^*F^\dagger\chi_l^* \tag{A27}$$

and

$$\sum_{u=1}^{4}A_uz_u^{-1}F\chi_u=\sum_{l=5}^{8}A_lM^*\chi_l^*. \tag{A28}$$

These give eight homogeneous equations in the eight unknowns and can only be solved when the corresponding determinant vanishes, which is the condition that E lies at a bound-state energy.

3. Method of solution

Equation (A10) can be written as two coupled equations

$$z^{-1}M\chi+\chi'=0, \tag{A29}$$

$$K\chi+zM^\dagger\chi-\chi'=0. \tag{A30}$$

These equations may be recast as the rank-8 system

$$\begin{pmatrix}z+NK & -N\\ M & z\end{pmatrix}\begin{pmatrix}\chi\\ \chi'\end{pmatrix}=0, \tag{A31}$$

where $N\equiv M^{\dagger-1}$. Thus the solutions z_j are the complex eigenvalues of the matrix

$$Q=\begin{pmatrix}-NK & N\\ -M & 0\end{pmatrix}\begin{pmatrix}\chi\\ \chi'\end{pmatrix}. \tag{A32}$$

Note that $\det(Q)=\det(M)\cdot\det(N)=1$ is independent of K and of the above-diagonal elements of M and the below-diagonal

elements of N. From row reduction, it is easy to derive

$$N = \frac{4}{\gamma_2\gamma_5}\begin{pmatrix} \frac{1}{2}\gamma_5 & 0 & 0 & 0 \\ 0 & \frac{1}{2}\gamma_2 & 0 & 0 \\ -\gamma_4 S^* & -\gamma_1\gamma_2\gamma_5^{-1} & \frac{1}{2}\gamma_2 & 0 \\ -\gamma_2^{-1}\gamma_3\gamma_5 S & \gamma_4 S^* & 0 & \frac{1}{2}\gamma_5 \end{pmatrix}. \tag{A33}$$

Equations (A27) and (A28) can now be written as an 8×8 system

$$\overbrace{\begin{pmatrix} M^{\dagger}_{ab}\xi_{bu} & -z_l^* F^{\dagger}_{ab}\xi^*_{bl} \\ z_u^{-1}F_{ab}\xi_{bu} & -M^*_{ab}\xi^*_{bl} \end{pmatrix}}^{R}\begin{pmatrix} A_{u=1,2,3,4} \\ A_{l=5,6,7,8} \end{pmatrix} = 0, \tag{A34}$$

where a, b, and u run from 1 to 4 and l runs from 5 to 8. The implied sums for each submatrix are over b and not u or l, and ξ_{ij} is the matrix of eigenvectors of Q,

$$\sum_{k=1}^{8} Q_{ik}\xi_{kj} = z_i\xi_{ij} \quad \text{(no sum on } i\text{)}, \tag{A35}$$

where i, j, and k run from 1 to 8. The bound-state condition is $\det(R)=0$.

We have numerically found the bound states lying in the gap between the bonding and antibonding π bands of graphite. Our results are displayed in Fig. 18. For the full SWMC calculation, there is no longer particle-hole symmetry. We find that the binding energy (i.e., the distance of the bound state from the closest band extremum) is considerable along the entire K-M edge. This is in contrast to our analytical results for the nearest-neighbor model, where the bound-state energy was considerable only for $|S|\approx\gamma_1/2\gamma_0\simeq 0.062$, which is satisfied only on a small ring about the K and K' points. On the other hand, the lack of bound states along the Γ-K edge implies a finite broadening of the Landau levels derived from this band.

It is important to realize that the SWMC model itself is only valid close to the K-H spine in the Brillouin zone. The model must be extended, as in Ref. 20, to include other tight-binding parameters in order to fit the π band throughout the entire zone, which is necessary in order to model various optical transitions. In this case, the in-plane hopping is modified as follows:

$$\gamma_0 S \to \gamma_0^{(1)} S_1 + \gamma_0^{(2)} S_2 + \gamma_0^{(3)} S_3, \tag{A36}$$

where $\gamma^{(n)}$ and S_n are, respectively, the amplitude and lattice sum of $e^{i\mathbf{k}\cdot\mathbf{ffi}}$ corresponding to the nth nearest-neighbor in-plane intersublattice hopping[20] subjected to the constraint

$$\gamma_0^{\mathrm{SWMC}} = \gamma_0^{(1)} - 2\gamma_0^{(2)} + \gamma_0^{(3)}. \tag{A37}$$

It is a rather simple matter to include such effects in our calculation, and we find in general for a broad set of possible parametrizations satisfying the constraint that our results have the same qualitative features.

Our approximations regarding the parameters Δ'' and $\tilde{\gamma}_4$ are such that, were their values known, our binding energies could easily be off by perhaps a few tens of millivolts. We expect, however, that the general features found here should still pertain, namely, a single bound state whose binding energy is maximized at several tens of millivolts along the K-M edge in the basal Brillouin zone.

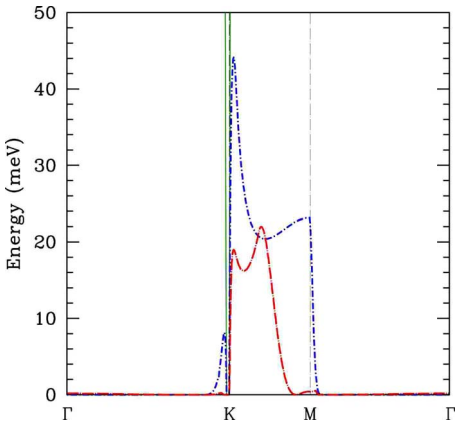

FIG. 18. (Color online) Binding energies for bound states within the gap at negative energies (blue short dash-dot curve) and positive energies (red long dash-dot curve), for the SWMC model with a single stacking fault, as a function of wave vector in the basal Brillouin zone. The solid green line shows the energy gap between bonding and antibonding π bands, which collapses in the vicinity of the basal zone corner K.

[1] A. H. Castro Neto, F. Guinea, N. M. R. Peres, K. S. Novoselov, and A. K. Geim, arXiv:0709.1163, Rev. Mod. Phys. (to be published), and references therein.

[2] N. B. Brandt, S. M. Chudinov, and Y. G. Ponomarev, *Semimetals I: Graphite and Its Compounds*, Modern Problems in Condensed Matter Sciences Vol. 20.1 (North Holland, Amsterdam, 1988).

[3] P. R. Wallace, Phys. Rev. **71**, 622 (1947); J. C. Slonczewski and P. R. Weiss, *ibid.* **109**, 272 (1958); J. W. McClure, *ibid.* **108**, 612 (1957); L. G. Johnson and G. Dresselhaus, Phys. Rev. B **7**, 2275 (1973).

[4] M. S. Dresselhaus and J. G. Mavroides, IBM J. Res. Dev. **8**, 262 (1964).

[5] B. A. Bernevig, T. L. Hughes, S. Raghu, and D. P. Arovas, Phys. Rev. Lett. **99**, 146804 (2007).

[6] B. I. Halperin, Jpn. J. Appl. Phys., Suppl. **26**, 1913 (1987); D. Poilblanc, G. Montambaux, M. Héritier, and P. Lederer, Phys. Rev. Lett. **58**, 270 (1987).

[7] D. J. Thouless, M. Kohmoto, M. P. Nightingale, and M. den Nijs, Phys. Rev. Lett. **49**, 405 (1982).

[8] J.-C. Charlier, X. Gonze, and J.-P. Michenaud, Carbon **32**, 289 (1994).

[9] S. Chehab, K. Guérin, J. Amiell, and S. Flandrois, Eur. Phys. J. B

13, 235 (2000).
[10] J. W. McClure, Carbon **7**, 425 (1969).
[11] Y. Hatsugai, Phys. Rev. B **48**, 11851 (1993).
[12] The value of the parameter γ_1 has been recently estimated from measurements in graphene bilayers. For ARPES measurements, see T. Ohta, A. Bostwick, T. Seyller, K. Horn, and E. Rotenberg, Science **313**, 951 (2006); for cyclotron effective masses, see E. V. Castro, K. S. Novoselov, S. V. Morozov, N. M. R. Peres, J. M. B. Lopes dos Santos, J. Nilsson, F. Guinea, A. K. Geim, and A. H. Castro Neto, Phys. Rev. Lett. **99**, 216802 (2007); and for optical absorption, see Z. Q. Li, E. Henriksen, Z. Jiang, Z. Hao, M. Martin, P. Kim, H. Stormer, and D. Basov, Nat. Phys. **4**, 532 (2008); and L. M. Zhang, Z. Q. Li, D. N. Basov, M. M. Fogler, Z. Hao, and M. C. Martin, Phys. Rev. B **78**, 235408 (2008), which are all consistent with the value of γ_1 in the range of 300–400 meV.
[13] D. R. Hofstadter, Phys. Rev. B **14**, 2239 (1976).
[14] Y. Kopelevich, J. H. S. Torres, R. R. da Silva, F. Mrowka, H. Kempa, and P. Esquinazi, Phys. Rev. Lett. **90**, 156402 (2003); H. Kempa, P. Esquinazi, and Y. Kopelevich, Solid State Commun. **138**, 118 (2006); Y. Kopelevich and P. Esquinazi, Adv. Mater. (Weinheim, Ger.) **19**, 4559 (2007).
[15] F. Guinea, A. H. Castro Neto, and N. M. R. Peres, Phys. Rev. B **73**, 245426 (2006).
[16] T. Matsui, H. Kambara, Y. Niimi, K. Tagami, M. Tsukada, and H. Fukuyama, Phys. Rev. Lett. **94**, 226403 (2005).
[17] Y. Niimi, H. Kambara, T. Matsui, D. Yoshioka, and H. Fukuyama, Phys. Rev. Lett. **97**, 236804 (2006).
[18] G. Li and E. V. Andrei, Nat. Phys. **3**, 623 (2007).
[19] M. S. Dresselhaus and G. Dresselhaus, Adv. Phys. **51**, 1 (2002).
[20] L. G. Johnson and G. Dresselhaus, Phys. Rev. B **7**, 2275 (1973).
[21] H. Chang and A. J. Bard, Langmuir **7**, 1143 (1991).
[22] S. R. Snyder, W. W. Gerberich, and H. S. White, Phys. Rev. B **47**, 10823 (1993).
[23] D. Yoshioka and H. Fukuyama, J. Phys. Soc. Jpn. **50**, 725 (1981); K. Takahashi and Y. Takada, Physica B **201**, 384 (1994).
[24] S. Tanuma, R. Inada, A. Furukawa, O. Takahashi, and Y. Iye, in *Physics in High Magnetic Fields*, edited by S. Chikazumi and N. Muira (Springer-Verlag, Berlin, 1981); Y. Iye, P. M. Berglund, and L. E. McNeil, Solid State Comm. **52**, 975 (1984).